Temperature and heat flux scaling laws for isoviscous, infinite Prandtl number mixed heating convection

Kenny Vilella and Frédéric Deschamps

Institute of Earth Sciences, Academia Sinica, 128, Section 2, Academia Rd, Nangang, Taipei 11529, Taiwan. E-mail: vilella@earth.sinica.edu.tw

SUMMARY

Thermal evolution of terrestrial planets is controlled by heat transfer through their silicate mantles. A suitable framework for modelling this heat transport is a system including bottom heating (from the core) and internal heating, for example, generated by secular cooling or by the decay of radioactive isotopes. The mechanism of heat transfer depends on the physical properties of the system. In systems where convection is able to operate, two different regimes are possible depending on the relative amount of bottom and internal heating. For moderate internal heating rates, the system is composed of active hot upwellings and cold downwellings. For large internal heating rates, the bottom heat flux becomes negative and the system is only composed of active cold downwellings. Here, we build theoretical scaling laws for both convective regimes following the approach of Vilella & Kaminski (2017), which links the surface heat flux and the temperature jump across both the top and the bottom thermal boundary layer (TBL) to the Rayleigh number and the dimensionless internal heating rate. Theoretical predictions are then verified against numerical simulations performed in 2-D and 3-D Cartesiangeometry, and covering a large range of the parameter space. Our theoretical scaling laws are more successful in predicting the thermal structure of systems with large internal heating rates than that of systems with no or moderate internal heating. The differences between moderate and large internal heating rates are interpreted as differences in the mechanisms generating thermal instabilities. We identified three mechanisms: conductive growth of the TBL, instability impacting, and TBL erosion, the last two being present only for moderate internal heating rates, in which hot plumes are generated at the bottom of the system and are able to reach the surface. Finally, we apply our scaling laws to the evolution of the early Earth, proposing a new model for the cooling of the primordial magma ocean that reconciles geochemical observations and magma ocean dynamics.

Key words: Mantle processes; Numerical modelling; Planetary interiors; Dynamics: convection currents, and mantle plumes; Dynamics of lithosphere and mantle; Heat generation and transport.

1 INTRODUCTION

Thermal convection controls the evolution of many natural systems with a large diversity of size and composition. In particular, in planetary bodies mantle convection governs the thermal evolution of the whole planets. Early studies considered Earth's mantle as a Rayleigh–Bénard convective system (e.g. McKenzie *et al.* 1973; Baumgardner 1985), namely a layer of fluid with constant temperature at both its top and bottom. The top temperature is set by the surface temperature and is lower than the bottom one, which is set by the temperature of the core. In this configuration, heat is coming from the bottom of the system, that is, in the case of the Earth, the core, and is transported by convective currents to the top of the mantle, where it is evacuated by conduction to the atmosphere

and oceans through the crust. Estimates of the mantle heat budget (Jaupart *et al.* 2015) show that bottom heating is small compared to volumetric (or internally generated) heating. In planetary mantles, the sources of volumetric heating are the decay of long-lived radioactive isotopes (^{238}U, ^{235}U ^{232}Th and ^{40}K) and secular cooling, which has been shown to be strictly equivalent to volumetric heating (Krishnamurti 1968; Daly 1980; Weinstein & Olson 1990). Mixed heating convective systems, that is, a convective system with both bottom and volumetric heating, therefore stand as a better reference system than Rayleigh–Bénard system to describe convection in the Earth's mantle.

Different approaches have been followed to estimate the thermal evolution of planetary mantles in the framework of mixed heating convection. A common approach is to use full numerical simulations

including several additional complexities, in particular compressibility, phase changes and temperature-dependent viscosity, and to compare the results of these simulations with observations (Machetel & Yuen 1989; Ogawa *et al.* 1991; Christensen & Hofmann 1994; Tackley *et al.* 1994; Tackley 1996). This method strongly depends on our knowledge of the system and on our ability to reproduce its complexity. Many successful applications have been achieved, including models of Earth's mantle explaining the current tomographic structure (e.g. Deschamps *et al.* 2015), and models of Moon's mantle explaining the evolution of surface volcanism (e.g. Laneuville *et al.* 2013). Alternatively, when the system is too complex to model, as in the case of plate tectonics on Earth (Jellinek & Jackson 2015), or poorly constrained, for example, models investigating the conditions required for habitability of exoplanets (Kite *et al.* 2009), the use of scaling laws is more appropriate. This parametrized convection approach relies on scaling laws linking the average surface heat flux and average thermal boundary layer (TBL) properties to the dimensionless numbers of the system (Sharpe & Peltier 1978; Christensen 1985).

Scaling laws have been established for many convective systems involving isoviscous fluids (e.g. Malkus 1954; Townsend 1964; Turcotte & Oxburgh 1967; Parmentier *et al.* 1994; Parmentier & Sotin 2000; Liu & Zhong 2013), fluids with strong variations of viscosity with temperature (e.g. Davaille & Jaupart 1993; Moresi & Solomatov 1995; Solomatov & Moresi 2000) or compressible fluids (e.g. Liu & Zhong 2013). For mixed heating convection in isoviscous, incompressible fluids, scaling laws have been established in Cartesian geometry (Sotin & Labrosse 1999; Moore 2008; Choblet & Parmentier 2009) and spherical geometry (Vangelov & Jarvis 1994; Jarvis *et al.* 1995; Shahnas *et al.* 2008; Deschamps *et al.* 2010; Choblet 2012; Weller *et al.* 2016). These studies provide relationships linking the average surface heat flux and temperature jump across the top TBL to the properties of the system, and more specifically its Rayleigh number, dimensionless heating rate and geometry. Predictions from scaling laws are very successful for characterizing mixed heating convection at moderate heating rates. At higher heating rates, the temperature of the convective interior becomes higher than the temperature at the bottom surface of the system, with the consequence that the system is cooled, instead of being heated, at its bottom. This specific convective regime, analogous to a purely volumetrically heated system, has not yet been studied in detail.

Here, we attempt developing a unifying theoretical framework for isoviscous fluids leading to scaling laws valid for mixed heating convection regardless of the values of the control parameters. Particular emphasis is placed on two peculiar end-member cases of mixed heating convection: bottom heating, that is, without volumetric heating; and volumetric heating, that is, for systems with an average bottom heat flux equal to zero. The volumetric heating case is somewhat similar to a pure volumetric heating system with an adiabatic bottom surface, that is, a system with a bottom heat flux equal to zero everywhere. Vilella & Kaminski (2017) developed a theoretical framework providing theoretical laws for a pure volumetric heating system with an adiabatic bottom surface. Here, we adapt this framework to bottom heated systems, and we then extend these scaling laws to mixed heated convection for both moderate (where the system is heated from below) and high (where the system is cooled from below) heating rates. This set of theoretical scaling laws is tested against 2-D and 3-D Cartesian numerical simulations. Interestingly, the scaling laws we obtain describe the thermal structure of the convective system dominated by volumetric heating (i.e. systems with large heating rates composed only of cold downwelling instabilities) better than that of other systems

(e.g. Rayleigh–Bénard system). Based on this result, we discuss the different possible mechanisms generating thermal instabilities. We conclude that the phenomenological model used to build our scaling laws, which was proposed by Howard (1966) and assumes that thermal instabilities are produced by the conductive growth of the TBL until it reaches a stability threshold, is only valid for convective systems without instabilities coming from the opposite TBL. In convective systems with one TBL at the top and one at the bottom, the two TBLs are coupled: conductive growth of instabilities in each TBL still occurs, but is perturbed by interactions with instabilities arriving from the opposite TBL. We finally apply our results to the evolution of early Earth, and we propose a model that reconciles geochemical observations and magma ocean dynamics.

2 THEORETICAL SCALING LAWS AT INFINITE PRANDTL NUMBER

2.1 Rayleigh–Bénard convection

Rayleigh–Bénard convection refers to a layer of fluid with constant temperature at top and bottom, the top temperature being lower than the bottom one. When considering an isoviscous and incompressible fluid, the convective system is controlled by two dimensionless numbers, the Rayleigh number,

$$Ra = \frac{\rho g \alpha \Delta T d^3}{\kappa \eta},$$ (1)

and the Prandtl number,

$$Pr = \frac{\eta/\rho}{\kappa},$$ (2)

where ρ is the density, g the acceleration of gravity, α the thermal expansion coefficient, ΔT the temperature jump across the fluid layer, d the layer thickness, η the dynamic viscosity and $\kappa = \lambda/\rho C_p$ the thermal diffusivity, with λ the thermal conductivity and C_p the heat capacity. In planetary bodies, the Prandtl number is very large ($Pr > 10^{20}$) and can be assumed effectively infinite, implying that the fluid acceleration has no significant effects on the evolution of the system and can be neglected. The convective system is, therefore, only controlled by its Rayleigh number.

The scaling laws and numerical simulations discussed in this study are based on a Cartesian geometry. By contrast, spherical geometry is often more appropriate in a planetary framework. Comparison between Cartesian and spherical geometry has been carried out for different convective systems (e.g. Deschamps *et al.* 2010; O'Farrell & Lowman 2010; O'Farrell *et al.* 2013; Weller *et al.* 2016). These studies have suggested that the scaling laws developed in Cartesian geometry are also valid in spherical geometry provided that a geometrical correction is applied. This correction is a function of the curvature (or equivalently, the ratio R_c/R_p where R_c and R_p are the radius of the core and the planet, respectively) and can be treated as a third dimensionless parameter. For the sake of simplicity, we therefore assume a Cartesian geometry, but note that similar reasoning may also be followed in spherical geometry.

For Ra lower than a critical value, denoted Ra_{cr}, the layer of fluid is in a purely conductive state. The value of Ra_{cr} can be calculated analytically for a 2-D infinite horizontal layer (Malkus 1954; Chandrasekhar 1961), and has been found to be about 657.5 in Cartesian system with free slip boundary conditions at top and bottom. For Ra larger than Ra_{cr}, convection starts and is characterized by two TBLs, one at the top and the other at the bottom, where a sharp change of temperature occurs. The system being symmetric, the

thermal structure of the two TBLs should be quantitatively similar. The fluid domain comprised between the two TBLs, hereafter called the convective interior, is composed of hot upwellings and cold downwellings transporting heat from the bottom to the top of the system throughout an otherwise adiabatic medium. For a given convective system, the size, number and distributions of upwellings and downwellings depend on the vigour of convection (Zhong 2005; Galsa & Lenkey 2007). Following the phenomenological model of Howard (1966), each TBL grows by conduction until it reaches a critical stage and breaks off to produce an instability, the bottom TBL producing hot instabilities (upwellings), and the top one, cold instabilities (downwellings).

Following an approach similar to that of Vilella & Kaminski (2017), which is itself based on the model of Howard (1966), we aim to establish theoretical scaling laws governing the convective system. In particular, we try to express the temperature jump across the TBL, $\Delta T_{\text{TBL, RB}}$, and its thickness, $\delta_{\text{TBL, RB}}$, as a function of Ra, which is the only dimensionless parameter of the system. As shown by Vilella & Kaminski (2017), due to the fact that a change in the TBL thickness, $\delta_{\text{TBL, RB}}$, is compensated by a change in the temperature jump across this TBL, $\Delta T_{\text{TBL, RB}}$, the Rayleigh number of each of the two TBLs, $Ra_{\text{TBL, RB}}$, is constant and thus does not depend on Ra. The value of $Ra_{\text{TBL, RB}}$ can be calculated, for instance, at the onset of convection, that is, for $Ra = Ra_{\text{cr}}$, because at that specific moment the system can still be approximated as conductive, while, at the same time and by definition, convection is beginning, thus implying the presence of TBLs. Assuming that at $Ra = Ra_{\text{cr}}$ the two TBLs extend over half of the fluid layer, implying $\Delta T_{\text{TBL, RB}} = 0.5 \, \Delta T$ and $\delta_{\text{TBL, RB}} = 0.5 \, d$, eq. (1) leads to

$$
\begin{aligned}
&Ra_{\text{TBL,RB}} \\
&= \frac{\rho g \alpha \, \Delta T_{\text{TBL,RB}} \delta_{\text{TBL,RB}}^3}{\kappa \eta} = \left(\frac{1}{2}\right)^4 \frac{\rho g \alpha \, \Delta T d^3}{\kappa \eta} = \left(\frac{1}{2}\right)^4 Ra_{\text{cr}}.
\end{aligned} \tag{3}
$$

For convenience $Ra_{\text{TBL, RB}}$ may further be written as a function of the properties (thickness and temperature contrast) of the TBL as follows:

$$
\begin{aligned}
Ra_{\text{TBL,RB}} &= \left(\frac{1}{2}\right)^4 Ra_{\text{cr}} \\
&= \frac{\rho g \alpha \, \Delta T_{\text{TBL,RB}} \delta_{\text{TBL,RB}}^3}{\kappa \eta} = Ra \left(\frac{\Delta T_{\text{TBL,RB}}}{\Delta T}\right)\left(\frac{\delta_{\text{TBL,RB}}}{d}\right)^3.
\end{aligned} \tag{4}
$$

Furthermore, the surface (or basal) heat flux, ϕ, which corresponds to the heat flux transported by the convective system, is determined by the conduction within the top (or bottom) TBL, and may thus be written as

$$
\phi \sim \lambda \frac{\Delta T_{\text{TBL,RB}}}{\delta_{\text{TBL,RB}}}, \tag{5}
$$

or,

$$
Nu_{\text{RB}} = \frac{\phi d}{\lambda \, \Delta T} = C_\phi \frac{\Delta T_{\text{TBL,RB}}}{\Delta T} \frac{d}{\delta_{\text{TBL,RB}}}, \tag{6}
$$

where Nu_{RB} is the Nusselt number, that is, the dimensionless convective heat flux, and C_ϕ a dimensionless constant. Combining eqs (4) and (6), we finally obtain that,

$$
\frac{\Delta T_{\text{TBL,RB}}}{\Delta T} = 0.5 \left(\frac{Nu_{\text{RB}}}{C_\phi}\right)^{3/4}\left(\frac{Ra}{Ra_{\text{cr}}}\right)^{-1/4}, \tag{7}
$$

and

$$
\frac{\delta_{\text{TBL,RB}}}{d} = 0.5 \left(\frac{Nu_{\text{RB}}}{C_\phi}\right)^{-1/4}\left(\frac{Ra}{Ra_{\text{cr}}}\right)^{-1/4}. \tag{8}
$$

Recalling that for $Ra = Ra_{\text{cr}}$, $\Delta T_{\text{TBL, RB}} = 0.5 \, \Delta T$, $\delta_{\text{TBL, RB}} = 0.5 \, d$ and $Nu_{\text{RB}} = 1$, eqs (7) and (8) imply $C_\phi = 1$. Eqs (7) and (8) constitute theoretical scaling laws that can be used to describe Rayleigh–Bénard convection provided that Nu_{RB}, which is a function of Ra, can be determined.

In order to estimate Nu_{RB}, we first note that eq. (7) implies that

$$
Nu_{\text{RB}}^{3/4} Ra^{-1/4} \sim \frac{\Delta T_{\text{TBL,RB}}}{\Delta T}. \tag{9}
$$

Furthermore, $\Delta T_{\text{TBL, RB}}/\Delta T$ should always be a finite value close to 0.5, while, when taking eq. (9) in the limit of an infinite Ra, this requires that Nu_{RB} scales as $Ra^{1/3}$, because otherwise $\Delta T_{\text{TBL, RB}}/\Delta T$ would either tend to zero or infinity. The scaling $Nu_{\text{RB}} \sim Ra^{1/3}$ is a well known result (e.g. Malkus 1954; Silveston 1958) that has been extensively validated by numerical simulations. There are, however, different ways to interpret this scaling. Here, we follow the formulation developed by Moore (2008) and write

$$
(Nu_{\text{RB}} - 1) \sim (Ra - Ra_{\text{cr}})^{1/3}. \tag{10}
$$

Note that for $Ra = Ra_{\text{cr}}$ the heat flux through the system is conductive, that is, $Nu_{\text{RB}} = 1$. A more convenient way to write eq. (10) is

$$
Nu_{\text{RB}} = 1 + C_N \left(\frac{Ra}{Ra_{\text{cr}}} - 1\right)^{1/3}, \tag{11}
$$

where C_N is not predicted by theoretical arguments, but can be constrained from numerical simulations (Section 3).

2.2 Mixed heating convection

Mixed heating convection refers to the bottom heating convection presented above with the addition of homogeneous volumetric heating. The convective system is controlled by the Rayleigh number, eq. (1), and the dimensionless heating rate,

$$
H = \frac{h d^2}{\lambda \Delta T}, \tag{12}
$$

where h is the dimensional internal heating rate per unit volume, which sets the relative importance of volumetric and bottom heating.

In the conductive state, the dimensionless conductive temperature profile in a plane layer is given by

$$
\frac{T(z)}{\Delta T} = \frac{T_{\text{surf}}}{\Delta T} - \frac{H}{2}z^2 + \left(\frac{H}{2} - 1\right)z + 1, \tag{13}
$$

where T_{surf} is the surface temperature and z is the dimensionless height. Interestingly, for H larger than 2, the heat flux at the bottom of the system is negative, meaning that the fluid cools down from both the top and the bottom. The change in sign of the basal heat flux also occurs when the system is animated by convection, but this requires $H > 2$. Two different convective regimes may therefore operate, depending on the value of H. For H lower than a critical threshold, hereafter denoted H_{crit}, the convective system has a positive heat flux at the bottom, and a TBL is present at both the top and the bottom of the system. In that case, the convective interior is composed of both downwelling and upwelling instabilities. The strength of upwelling instabilities (hot plumes) decreases as the value of H approaches H_{crit}, that is, that the temperature jump across the bottom TBL is reduced. The hot plumes are then weaker and may not reach the surface (Travis & Olson 1994; Sotin & Labrosse 1999; Deschamps et al. 2010). For H equal to or larger than H_{crit}, the bottom heat flux becomes zero or negative, and a conductive, stable, layer forms at the bottom of the system. The convective interior is then composed

of downwelling instabilities and a non-buoyant return flow. This behaviour has also been reported for volumetric heating system with an adiabatic bottom surface. Note that, because the amount of heat transported by the system increases with Ra, the value of H_{crit} is also expected to increase with Ra (Sotin & Labrosse 1999; Deschamps *et al.* 2010; O'Farrell & Lowman 2010). We now examine these two cases, $H \le H_{crit}$ and $H \ge H_{crit}$, in more detail.

2.2.1 Case $H \le H_{crit}$

In this section, we aim to establish scaling laws for the convective system when H is lower than H_{crit}. We note ϕ the top heat flux, Nu_t its dimensionless value, that is, $Nu_t = \phi d / \lambda \Delta T$, and we assume that Nu_t is the sum of two components,

$$Nu_t = f(Ra) + g(H), \tag{14}$$

where f and g are two functions describing the fractions of the surface heat flux due to bottom heating and internal heating, respectively, with f being a function of Ra only, and g a function of H only. Since the surface heat flux should be directly related to the amount of heat internally generated, we furthermore consider that g is a linear function of H, $g(H) = C_g H$, with C_g a dimensionless constant between zero and one. When $H = H_{crit}$, the bottom heat flux is equal to zero, the conservation of energy, therefore, requires that the surface heat flux is equal to the heat internally generated, that is, $Nu_t(H = H_{crit}) = H_{crit}$. Using eq. (14), we then obtain that at $H = H_{crit}$.

$$f(Ra) = (1 - C_g)H_{crit}, \tag{15}$$

where H_{crit} is a function of Ra that needs to be determined. Eq. (14) therefore implies

$$Nu_t = (1 - C_g)H_{crit} + C_g H. \tag{16}$$

Another constraint is given by the value of H_{crit} at $Ra = Ra_{cr}$, which, according to eq. (13), should be equal to 2. Considering the case $Ra = Ra_{cr}$, implying $Nu_t = 1$ for a Cartesian geometry, and $H = 0$, we obtain $C_g = 1/2$, or

$$Nu_t = \frac{1}{2}(H + H_{crit}). \tag{17}$$

Note that Moore (2008) obtained a similar result. An interesting implication of eq. (17) is that the dimensionless surface heat flux in Rayleigh–Bénard convection ($H = 0$) is equal to $0.5 H_{crit}$. When $H = 0$, $Nu_t = Nu_{RB}$, and combining eqs (11) and (17) gives

$$H_{crit} = 2\, Nu_{RB} = 2 + 2\, C_N \left(\frac{Ra}{Ra_{cr}} - 1 \right)^{1/3}. \tag{18}$$

We now aim to establish a scaling law linking the temperature jump across the top TBL, $\Delta T_{TBL,t}$, to the dimensionless parameters of the system, here Ra and H. As a first step, we perform a scaling analysis similar to that conducted by Vilella & Kaminski (2017) in the purely internally heated case. First, we note that within the TBL, heat is transferred by conduction, implying that the surface heat flux scales as

$$\phi \sim \lambda \frac{\Delta T_{TBL,t}}{\delta_{TBL,t}}, \tag{19}$$

where $\delta_{TBL,t}$ is the thickness of the top TBL. Following Howard (1966), we then consider the dynamics of the TBL just before it becomes unstable. At that stage, the thickness of the TBL is such that there is a balance between the buoyancy force, which drives the convective flow, and the viscous drag that prevents the destabilization

of the layer, that is,

$$\rho \alpha g \Delta T_{TBL,t} \sim \eta \frac{w}{\delta_{TBL,t}^2}, \tag{20}$$

where w is a vertical velocity scale that remains to be determined. To obtain w, we use the equation of conservation of energy in the convective system,

$$\rho C_P \frac{DT}{Dt} = \lambda \nabla^2 T + h, \tag{21}$$

where DT/Dt is the material derivative of the temperature. In the convective fluid just underneath the base of the TBL, that is, where $T(z = d - \delta_{TBL,t}) = \Delta T_{TBL,t}$, conduction is negligible, and the vertical advection of heat balances heat production, leading to

$$\rho C_P \frac{w \Delta T_{TBL,t}}{d} \sim h. \tag{22}$$

Combining eqs (20) and (22), we obtain

$$\rho \alpha g \Delta T_{TBL,t}^2 \delta_{TBL,t}^2 \sim \frac{\eta h d}{\rho C_P}. \tag{23}$$

Finally, together with eq. (19) and the definition of the dimensionless numbers (Ra, H and Nu_t), eq. (23) provides a scaling for the temperature jump in the top TBL,

$$\frac{\Delta T_{TBL,t}}{\Delta T} \sim H^{1/4} Nu_t^{1/2} Ra^{-1/4}. \tag{24}$$

This scaling as well as eq. (22) is only valid when internal heating is dominant, since, for $H = 0$, eq. (24) predicts that the dimensionless temperature jump across the top TBL, $\Delta T_{TBL,t}/\Delta T$ is equal to zero, which is incorrect. In order to establish a scaling consistent with values of H equal or close to zero, we define a more general form of eq. (24),

$$\frac{\Delta T_{TBL,t}}{\Delta T} = f_t(Ra) + g_t(Ra)\, H^{1/4} Nu_t^{1/2} Ra^{-1/4}, \tag{25}$$

where $f_t(Ra)$ and $g_t(Ra)$ are two unknown dimensionless functions. The first term in the right-hand side of eq. (25) may be obtained by setting $H = 0$, which is equivalent to Rayleigh–Bénard convection, and by using the scaling law [eq. (7)] together with eq. (18), we get

$$f_t(Ra) = 0.5 \left(\frac{H_{crit}}{2\, C_\phi} \right)^{3/4} \left(\frac{Ra}{Ra_{cr}} \right)^{-1/4}. \tag{26}$$

To determine $g_t(Ra)$, we use the fact that for $H = H_{crit}$ the convective system is equivalent to internally heated convection and should satisfy the scaling determined in eq. (24). Therefore,

$$C_T H_{crit}^{1/4} Nu_t^{1/2} Ra^{-1/4} = f_t(Ra) + g_t(Ra)\, H_{crit}^{1/4} Nu_t^{1/2} Ra^{-1/4}, \tag{27}$$

where C_T is a dimensionless constant, and

$$g_t(Ra) = -(f_t(Ra) - C_T H_{crit}^{1/4} Nu_t^{1/2} Ra^{-1/4})\, H_{crit}^{-1/4} Nu_t^{-1/2} Ra^{1/4}. \tag{28}$$

Combining eqs (28), (26) and (25), we finally obtain

$$\frac{\Delta T_{TBL,t}}{\Delta T} = 0.5 \left(\frac{H_{crit}}{2\, C_\phi} \right)^{3/4} \left(\frac{Ra}{Ra_{cr}} \right)^{-1/4} \left(1 - \left(\frac{H}{H_{crit}} \right)^{1/4} \right) + C_T H^{1/4} Nu_t^{1/2} Ra^{-1/4}. \tag{29}$$

Moreover, for $Ra = Ra_{cr}$ and $H = 2$, the temperature jump in the top TBL is equal to the total temperature jump across the system, $\Delta T_{TBL,t}/\Delta T = 1$, allowing the determination of C_T. The temperature

jump in the top TBL is then fully described by

$$\frac{\Delta T_{\text{TBL,t}}}{\Delta T} = 0.5 \left(\frac{H_{\text{crit}}}{2\,C_\phi}\right)^{3/4} \left(\frac{Ra}{Ra_{\text{cr}}}\right)^{-1/4} \left(1 - \left(\frac{H}{H_{\text{crit}}}\right)^{1/4}\right)$$
$$+ \left(\frac{H}{2}\right)^{1/4} \left(\frac{Nu_t}{2}\right)^{1/2} \left(\frac{Ra}{Ra_{\text{cr}}}\right)^{-1/4}, \quad (30)$$

where, as previously mentioned, $C_\phi = 1$ in Cartesian geometry.

We now follow a similar approach to characterize the bottom TBL, which has a very different behaviour from the top one. With increasing H, the internal heating becomes the dominant source of heating, implying that the dynamics of the top TBL is mostly controlled by conductive growth of thermal instabilities, as in the case of purely internally heated convection. By contrast, increasing the amount of internal heating behaves as a stability factor for the bottom TBL, and consequently the scaling obtained in eq. (24) is no longer relevant. Based on the scaling analysis conducted for the top TBL, we assume that

$$\frac{\Delta T_{\text{TBL,b}}}{\Delta T} = f_{\text{b}}(Ra) + C_{\text{b}} H^\beta Nu_{\text{b}}^\theta Ra^\gamma, \quad (31)$$

where the subscript b means bottom, $f_{\text{b}}(Ra)$ is again an unknown dimensionless function, and C_{b}, β, θ and γ are dimensionless constants. At $H = 0$, the system is equivalent to a Rayleigh–Bénard convective system, for which the temperature scaling has been determined [eq. (7)]. In the case $\beta = 0$ and $H = 0$, using eqs (7), (18) and (31) we can write

$$0.5 \left(\frac{H_{\text{crit}}}{2\,C_\phi}\right)^{3/4} \left(\frac{Ra}{Ra_{\text{cr}}}\right)^{-1/4} = f_{\text{b}}(Ra) + C_{\text{b}} Nu_{\text{b}}^\theta Ra^\gamma, \quad (32)$$

implying

$$\frac{\Delta T_{\text{TBL,b}}}{\Delta T} = 0.5 \left(\frac{H_{\text{crit}}}{2\,C_\phi}\right)^{3/4} \left(\frac{Ra}{Ra_{\text{cr}}}\right)^{-1/4}. \quad (33)$$

For $H = H_{\text{crit}}$, the temperature jump should be zero, which is not predicted by eq. (33). Therefore, β should not be equal to zero. If $H = 0$, and using eqs (7) and (18), eq. (31) requires that,

$$f_{\text{b}}(Ra) = 0.5 \left(\frac{H_{\text{crit}}}{2\,C_\phi}\right)^{3/4} \left(\frac{Ra}{Ra_{\text{cr}}}\right)^{-1/4}. \quad (34)$$

Considering the case $H = H_{\text{crit}}$, eqs (31) and (34) thus yield

$$0 = 0.5 \left(\frac{H_{\text{crit}}}{2\,C_\phi}\right)^{3/4} \left(\frac{Ra}{Ra_{\text{cr}}}\right)^{-1/4} + C_{\text{b}} H_{\text{crit}}^\beta Nu_{\text{b}}^\theta Ra^\gamma. \quad (35)$$

Because for $H = H_{\text{crit}}$ the dimensionless bottom heat flux is, by definition, equal to zero ($Nu_{\text{b}} = 0$), eq. (35) is true only if $\theta = 0$. For $\theta = 0$ and because C_{b} is a constant, eq. (35) requires that $\beta = 3/4$, $\gamma = -1/4$ and $C_{\text{b}} = -0.5\,(2\,C_\phi)^{-3/4}\,Ra_{\text{cr}}^{1/4}$. Inserting these values in eq. (31) and using eq. (34), we finally obtain,

$$\frac{\Delta T_{\text{TBL,b}}}{\Delta T} = 0.5 \left[\left(\frac{H_{\text{crit}}}{2\,C_\phi}\right)^{3/4} - \left(\frac{H}{2\,C_\phi}\right)^{3/4}\right] \left(\frac{Ra}{Ra_{\text{cr}}}\right)^{-1/4}, \quad (36)$$

where, again, $C_\phi = 1$ in Cartesian geometry. Eqs (30) and (36) establish scaling laws linking the temperature across the top and bottom TBL to the input parameters of the convective system for the case $H < H_{\text{crit}}$.

2.2.2 Case $H \geq H_{\text{crit}}$

In this regime, a subadiabatic conductive layer of thickness δ_b is generated at the bottom of the system, and convection is limited to the region located above this subadiabatic layer. The heat generated in this conductive layer escapes at the bottom of the system and does not participate in convection. This 'lost' heat should not be considered when establishing the thermal structure of the top TBL. To account for it, we replace the parameter H by $H_{\text{eff}} = (1 - \delta_b/d)H$, representing the effective amount of heat driving convection for a Cartesian geometry. Interestingly, in this case there is no heat coming from the bottom conductive layer, and the top heat flux Nu_t is simply equal to H_{eff}. We, therefore, assume that the scaling law characterizing the top TBL determined for $H < H_{\text{crit}}$ remains valid for $H > H_{\text{crit}}$, except that H is replaced by H_{eff} (or equivalently, the top dimensionless heat flux Nu_t). Thus, following eq. (30) we obtain

$$\frac{\Delta T_{\text{TBL,t}}}{\Delta T} = 0.5 \left(\frac{H_{\text{crit}}}{2\,C_\phi}\right)^{3/4} \left(\frac{Ra}{Ra_{\text{cr}}}\right)^{-1/4} \left(1 - \left(\frac{Nu_t}{H_{\text{crit}}}\right)^{1/4}\right)$$
$$+ \left(\frac{Nu_t}{2}\right)^{3/4} \left(\frac{Ra}{Ra_{\text{cr}}}\right)^{-1/4}. \quad (37)$$

Unfortunately, the same process is unlikely to be valid for the bottom TBL. At the bottom, the mechanism of heat transfer changes from convection, at $H < H_{\text{crit}}$, to conduction, at $H > H_{\text{crit}}$, while the scaling analysis conducted above is only valid for convection. This implies that a different approach should be followed. Moreover, our numerical simulations (Section 3) suggest that the temperature jump across the conductive bottom is set by the convective interior. A scaling analysis for this case is thus challenging. Alternatively, we note that the temperature jump across the conductive bottom cannot be larger than the temperature jump across the top TBL, because in convective systems dominated by volumetric heating, the highest temperature of the system is located just beneath the top TBL (e.g. Parmentier & Sotin 2000). In addition, the temperature of the convective interior, that is, the domain comprised between the top TBL and the conductive bottom, should be almost constant due to adiabaticity. However, experiments and numerical simulations show that, for mixed heating systems, temperature slightly decreases with depth (i.e. subadiabatic), due to the effect of cold downwellings (Jeanloz & Morris 1987; Sinha & Butler 2007). These observations suggest that the temperature jump across the conductive bottom is slightly lower than the temperature jump across the top TBL. Based on empirical observations, detailed and tested in Section 3, we assume that the ratio of the temperature jump across the top TBL over the temperature jump across the conductive bottom depends only on the Rayleigh number. Thus, this ratio does not depend on H and may be written at any value of this parameter, for instance, for $H = H_{\text{crit}}$,

$$\frac{\Delta T_{\text{TBL,t}}(Ra, H)}{\Delta T_{\text{b}}(Ra, H)} = \frac{\Delta T_{\text{TBL,t}}(Ra, H = H_{\text{crit}})}{\Delta T_{\text{b}}(Ra, H = H_{\text{crit}})}, \quad (38)$$

where ΔT_{b} is the temperature jump across the convective layer, that is, between the surface and the top of the conductive layer such that $\Delta T_{\text{b}} = \Delta T + \Delta T_{\text{TBL,b}}$. We further note that $\Delta T_{\text{b}}(Ra, H = H_{\text{crit}}) = \Delta T$, the temperature at the bottom boundary, while $\Delta T_{\text{TBL,t}}$ at (Ra, H) and $(Ra, H = H_{\text{crit}})$ are given by eq. (37), so that the only unknown in eq. (38) is ΔT_{b} at (Ra, H), therefore requiring that

$$\frac{\Delta T_{\text{b}}}{\Delta T} = \frac{0.5}{C_\phi^{3/4}} \left(1 - \left(\frac{Nu_t}{H_{\text{crit}}}\right)^{1/4}\right) + \left(\frac{Nu_t}{H_{\text{crit}}}\right)^{3/4}. \quad (39)$$

Interestingly, the conductive bottom follows a conductive temperature profile [the general form of which is being given in eq. (13) for a Cartesian geometry], and this profile gives a direct relationship between the temperature jump across the conductive bottom and the

bottom heat flux,

$$\frac{\Delta T_{TBL,b}}{\Delta T} = \frac{\delta_b}{d}\left(Nu_b - 0.5\,H\frac{\delta_b}{d}\right), \tag{40}$$

with δ_b the thickness of the conductive bottom. We further assume that the bottom heat flux is equal to the heat generated within the conductive bottom, that is, $Nu_b = H\delta_b/d$, and obtain

$$Nu_b = \left(2\frac{\Delta T_{TBL,b}}{\Delta T}H\right)^{1/2}. \tag{41}$$

Conservation of energy then gives the top heat flux, and therefore the effective internal heating, H_{eff},

$$Nu_t = H_{eff} = H - \left(2\frac{\Delta T_{TBL,b}}{\Delta T}H\right)^{1/2}. \tag{42}$$

Solving eqs (39) and (42) provides a theoretical prediction for the surface heat flux.

Table 1 summarizes the theoretical scaling laws we derived for the surface heat flux and thermal structure of the TBL in the case of mixed heating convection. Note that the estimation of H_{crit} still relies on the determination of an empirical constant, C_N, which is not related to some theoretical arguments, but may be adjusted by comparison with numerical experiments. In that sense, our scaling laws are not strictly theoretical. However, H_{crit} is a physical property of the system that can be measured, and not a dimensionless constant free to vary. In the next section, we test our scaling laws against numerical simulations.

3 TESTING THEORETICAL SCALING LAWS AGAINST NUMERICAL SIMULATIONS

3.1 Numerical model

We performed numerical experiments using the code StagYY (Tackley *et al.* 1994; Tackley 2008) in both 2-D and 3-D Cartesiangeometry. This code uses a finite difference multigrid technique to solve the conservation equations of mass, momentum and energy on a staggered grid. We consider a layer of fluid internally heated with constant temperature at the surface and at the base, and that is fully characterized by its Rayleigh number, Ra, and its amount of internal heating, H. The side boundaries are reflecting, while the top and bottom boundary conditions are free slip. We use a constant temperature in the whole box with random perturbations as the initial temperature condition. A statistical steady state is reached when both the volumetric average temperature and the surface heat flux are constant (i.e. their fluctuations are zero) when averaged over several overturn times.

The selected aspect ratio and the space resolution of the grid (Table 2) guarantee both the development of well-developed convective currents, and a good resolution of the TBLs. For some cases, the results obtained in 2-D Cartesiangeometry indicated an important wall-effect caused by the geometry (Cross & Hohenberg 1993), even for large aspect ratio. For those cases, we ran the equivalent 3-D Cartesiangeometry simulation to obtain robust results. We also conducted a few additional 3-D Cartesiangeometry simulations to gauge the effect of changing the geometry, that is, from 2-D to 3-D, on our results. In particular, we have conducted three numerical simulations at $Ra = 10^7$ and $H = 0$, two in 2-D geometry and one in 3-D geometry. Some differences can be observed in Table 2 between the numerical simulations. Part of the differences is due to

the horizontal resolution, as can be seen by the comparison between the two numerical simulations in 2-D geometry. Another important factor is the total duration of simulations. Because of the chaotic nature of thermal convection, the flow pattern experiences temporal variations with both short-period and long-period. 3-D numerical simulations with high lateral and vertical resolutions are usually conducted for shorter durations than 2-D simulations with similar properties. If too short, 3-D simulations may not, in some cases, entirely capture long-term temporal variations. By contrast, numerical simulations in 2-D can be conducted over a much longer period of time and with higher resolutions. Note, however, that the differences observed between the three cases are less than 10 per cent, and agree within their temporal fluctuations.

3.2 Comparison between theory and numerical simulations

The theoretical framework we developed in Section 2 is built upon critical numbers, Ra_{cr} and H_{crit}, that control the main properties of the system. Values of Ra_{cr} have been calculated analytically for a large diversity of systems. However, at that point, H_{crit} cannot be determined entirely from theoretical arguments, and an empirical constant needs to be determined by fitting numerical simulations or laboratory experiments. An estimate of H_{crit} has been proposed by Moore (2008), and here we refine this estimate by combining previous numerical simulations (Sotin & Labrosse 1999; Moore 2008) with a new set of numerical simulations specifically conducted for the determination of H_{crit} (Table 2). The results shown in Fig. 1(a) exhibit a fairly good agreement between our scaling law with $C_N = 1.5$ and the numerical results. An interesting output of our theoretical scalings is that the Nusselt number for Rayleigh–Bénard convection is equal to $0.5\,H_{crit}$. We verify this property in Fig. 1(b). One may note that the interior temperature in Rayleigh–Bénard convection is larger than the surface temperature by $0.5\,\Delta T$, implying $\phi \approx 0.5\,\lambda\Delta T/\delta_{TBL,RB}$ and $Nu_{RB} \approx 0.5\,d/\delta_{TBL,RB}$, while for $H = H_{crit}$ the interior temperature is larger than the surface temperature by about ΔT, implying $\phi \approx \lambda\Delta T/\delta_{TBL,t}$ and $Nu_t = H_{crit} \approx d/\delta_{TBL,t}$. Assuming that at a given Ra, $\delta_{TBL,RB} \approx \delta_{TBL,t}$, one gets $Nu_{RB} \approx 0.5\,d/\delta_{TBL,RB} \approx 0.5\,d/\delta_{TBL,t} \approx 0.5Nu_t$, which provides a first order justification for the result $Nu_{RB} = 0.5\,H_{crit}$.

We first check the validity of the scaling laws proposed in Section 2.2.1 for the case $H \leq H_{crit}$. A comparison with the scaling laws established by Moore (2008) is further conducted in the Supporting Information. To quantify the fit between numerical simulations and our scaling laws, we calculate the coefficient of determination R^2 defined as

$$R^2 = 1 - \frac{\sum\limits_{i=1}^{n}(m_i - p_i)^2}{\sum\limits_{i=1}^{n}(m_i - m_{avg})^2} \tag{43}$$

where n is the number of data points, $m_{1,\,..,\,n}$ the measured values, $p_{1,\,..,\,n}$ the predicted values and m_{avg} the average value of $m_{1,\,..,\,n}$. The measure of the surface heat flux is straightforward and the results are reported in Fig. 2(a). Despite the large error bars, due to temporal variations of the surface heat flux in 2-D geometry, the agreement between predictions and measurements is very good, with $R^2 = 0.9904$, thus supporting our approach. It should be kept in mind that this scaling law only relies on the empirical determination of H_{crit} and does not require any additional fitting parameter, making the agreement even more striking. The empirical determination of the temperature jump across both TBLs is more difficult. Most

Table 1. Scaling laws for temperature jump across the top and bottom thermal boundary layer, surface heat flux and critical heating rate, H_{crit}, that is, the heating rate for which the bottom heat flux goes to zero. Note that $\Delta T_b = \Delta T + \Delta T_{TBL,b}$ is the temperature jump across the convective layer, that is, between the surface and the top of the conductive layer. C_N is a dimensionless constant introduced in eq. (11) and assumed to be equal to 1.5 based on its empirical determination in Fig. 1(a), while C_ϕ is a dimensionless constant introduced in eq. (7) and found theoretically to be equal to 1 in Cartesian geometry.

Parameter	Scaling	Equation
Critical heating rate	$H_{crit} = 2 + 2C_N(\frac{Ra}{Ra_{cr}} - 1)^{1/3}$	(18)
Top temperature jump		
$H \leq H_{crit}$	$\frac{\Delta T_{TBL,t}}{\Delta T} = 0.5(\frac{H_{crit}}{2C_\phi})^{3/4}(\frac{Ra}{Ra_{cr}})^{-1/4}(1 - (\frac{H}{H_{crit}})^{1/4})$ $+ (\frac{H}{2})^{1/4}(\frac{Nu_t}{2})^{1/2}(\frac{Ra}{Ra_{cr}})^{-1/4}$	(30)
$H \geq H_{crit}$	$\frac{\Delta T_{TBL,t}}{\Delta T} = 0.5(\frac{H_{crit}}{2C_\phi})^{3/4}(\frac{Ra}{Ra_{cr}})^{-1/4}(1 - (\frac{Nu_t}{H_{crit}})^{1/4})$ $+ (\frac{Nu_t}{2})^{3/4}(\frac{Ra}{Ra_{cr}})^{-1/4}$	(37)
Bottom temperature jump		
$H \leq H_{crit}$	$\frac{\Delta T_{TBL,b}}{\Delta T} = 0.5[(\frac{H_{crit}}{2C_\phi})^{3/4} - (\frac{H}{2C_\phi})^{3/4}](\frac{Ra}{Ra_{cr}})^{-1/4}$	(36)
$H \geq H_{crit}$	$\frac{\Delta T_b}{\Delta T} = \frac{0.5}{C_\phi^{3/4}}(1 - (\frac{Nu_t}{H_{crit}})^{1/4}) + (\frac{Nu_t}{H_{crit}})^{3/4}$	(39)
Surface heat flux		
$H \leq H_{crit}$	$Nu_t = \frac{1}{2}(H + H_{crit})$	(17)
$H \geq H_{crit}$	$Nu_t = H - (2\frac{\Delta T_{TBL,b}}{\Delta T}H)^{1/2}$	(42)

previous studies used the horizontally averaged temperature profile to visualize the top TBL. Recently, Vilella & Kaminski (2017) used the hot temperature profile, defined as the profile of the maximum temperature at each depth, arguing that this temperature profile is more appropriate for visualizing the critical TBL. Using this hot profile, the base of the TBL can be defined using various methods leading to slightly different results. However, for establishing eq. (22), we explicitly defined the base of the TBL as the location where conduction becomes negligible, corresponding to the depth at which the first derivative of the temperature with respect to depth becomes negligible. The method we select must, therefore, be consistent with this previous definition. For consistency, we here fix the base of the TBL at the closest point to the boundary where the first derivative of temperature (T'), that is, heat conduction, reaches 1 per cent of its minimum or maximum value. For instance, for the top TBL, this corresponds to the largest value of the dimensionless height z for which $T'(z) > 0.01 \min(T')$.

Fig. 2(b) compares the numerical results against the theoretical predictions for $\Delta T_{TBL,t}$, and shows that the predicted temperatures are systematically higher than the observed ones, except for the cases conducted with $H \approx 0$. The disagreement is rather small, but large enough to be significant. Defining the base of the TBL differently may improve the results, but the disagreement is large enough to persist. For $\Delta T_{TBL,b}$, the discrepancies between predicted and observed values are even worse, and predictions are decorrelated from observations. Our theoretical framework, thus, globally fails in predicting the thermal structure of the system for $H \leq H_{crit}$. These discrepancies might be related to the fact that the scaling law we obtained does not account for the interactions between the instabilities growing in the TBL and the plumes coming from the opposite TBL (Section 4).

For mixed heating convection with $H \geq H_{crit}$, the convective regime is radically different and the scaling law for $\Delta T_{TBL,b}$ is obtained assuming that the ratio of the temperature jump across the top TBL over the temperature jump across the conductive bottom depends only on the Rayleigh number. To verify that this assumption is correct we compared the temperature profiles obtained at $Ra = 10^4$ and $Ra = 10^7$ with various values of H (Fig. 3). In Fig. 3, we observe slight variations of the temperature ratio in the convective interior that may be related to 2-D geometry effects. 3-D numerical

simulations would give better results but are extremely time consuming and challenging for such high values of H. Nevertheless, Fig. 3 indicates that our assumption is appropriate. Fig. 3 also shows that identifying the bottom conductive layer is a difficult issue. We first note that the horizontally averaged temperature profile is more appropriate than the hot temperature profile to identify the upper limit of the bottom conductive layer. The hot temperature profile is used to select precisely the TBL at its critical stage just before its destabilization, while the horizontally averaged profile averages out the TBL at different stages of its evolution. However, the bottom conductive layer does not evolve with time but is occasionally disturbed by cold downwellings that push hot materials to the bottom of the system. In that case, it is therefore more appropriate to use the horizontally averaged profile. To identify the upper limit of the bottom conductive layer, we then simply make use of the conductive nature of this layer. More specifically, we proceed in two steps. First, we best-fit the bottom conductive layer with a conductive profile [the general form of which is being given in eq. (13)]. We then search for the closest point to the bottom boundary where the actual temperature profile differs from the fitted conductive profile by more than 1 per cent. This difference indicates that the fluid is diverging from the purely conductive state, and therefore denotes the upper limit of the bottom conductive layer. This method has the advantage to be fully coherent with the framework used to establish our theoretical predictions (eq. 39). Note that the method used for determining the base of the top TBL remains the same as the one used for $H \leq H_{crit}$. Fig. 4, comparing measurements and predictions, indicates that our scaling laws are in very good agreement with numerical simulations, with R^2 very close to 1. These scaling laws are even valid for extreme values of H, yielding values of the internal temperature up to 16 times the imposed temperature jump between the surface and the base of the box. Although truncated in Fig. 4(a) for graphical reasons, the surface heat flux is correctly predicted for dimensionless values up to 2800. The scaling laws presented in this work, therefore, successfully predict the surface heat flux and thermal structure of mixed heating convection for $H \geq H_{crit}$. To our knowledge, no previous scaling was able to achieve this.

A curious characteristic of our theoretical framework is that the scaling laws for $H \leq H_{crit}$ failed to predict correctly the thermal structure of the system, while in the meantime they are also used to

Table 2. Input parameters and output observables of the numerical simulations performed in this study. Note that for $H \geq H_{crit}$ we report the value of $\Delta T_b = \Delta T + \Delta T_{TBL, b}$ instead of the value of $\Delta T_{TBL, b}$.

Ra	H	Resolution	Aspect ratio	$\Delta T_{TBL, t}$	$\Delta T_{TBL, b}$ or ΔT_b	Nu_t
10^4	0	$1024 \times 1024 \times 64$	32:32	0.946	0.947	4.369
10^4	0.5	512×64	16	0.802	0.747	5.171
10^4	1	512×64	16	0.821	0.717	5.419
10^4	5	$512 \times 512 \times 64$	16:16	1.194	0.859	6.702
10^4	6	$512 \times 512 \times 64$	16:16	1.283	0.820	7.215
10^4	8	$512 \times 512 \times 64$	16:16	1.425	0.715	8.161
10^4	8.5	$512 \times 512 \times 64$	16:16	1.497	0.718	8.469
10^4	9	$512 \times 512 \times 64$	16:16	1.507	0.748	8.787
10^4	9.5	$512 \times 512 \times 64$	16:16	1.525	1.007	9.111
10^4	10	512×64	16	1.625	1.033	8.991
10^4	25	1024×128	16	2.651	1.653	18.684
10^4	50	768×192	8	4.187	2.654	35.619
10^4	100	768×192	8	7.090	4.407	70.841
10^4	200	768×192	8	11.87	7.436	143.56
10^4	200	$768 \times 768 \times 192$	8:8	11.42	6.623	149.21
10^4	300	768×192	8	16.04	10.75	218.17
2×10^4	8	$512 \times 512 \times 64$	16:16	1.311	0.797	9.185
3×10^4	5	$512 \times 512 \times 64$	16:16	1.044	0.854	8.387
10^5	1	1024×128	16	0.921	0.849	8.935
10^5	1	$1024 \times 1024 \times 128$	8:8	0.969	0.899	9.624
10^5	10	1024×128	16	1.105	0.633	12.932
10^5	18	1024×128	16	1.489	1.026	17.082
10^5	19	3072×192	32	1.483	1.037	17.719
10^5	20	1024×128	16	1.540	1.056	18.559
10^5	50	3072×192	32	2.580	1.727	40.427
10^6	0	$1024 \times 1024 \times 512$	6:6	0.967	0.949	19.714
10^6	10	512×128	8	0.877	0.741	21.992
10^6	20	$512 \times 512 \times 128$	8:8	1.029	0.742	28.655
10^6	30	512×128	8	1.183	0.273	32.327
10^6	35	512×128	8	1.253	0.267	35.523
10^6	36	1536×384	8	1.277	0.352	36.153
10^6	37	512×128	8	1.290	0.996	36.824
10^6	100	1536×384	8	2.406	1.744	86.076
10^7	0	$1024 \times 1024 \times 512$	8:8	0.954	0.939	41.537
10^7	0	1028×512	8	0.839	0.802	37.229
10^7	0	2048×512	8	0.890	0.811	36.077
10^7	1	2048×512	8	0.852	0.742	36.246
10^7	5	2048×512	8	0.840	0.846	37.324
10^7	10	2048×512	8	0.839	0.558	39.280
10^7	20	2048×512	8	0.865	0.629	42.902
10^7	30	2048×512	8	0.887	0.566	48.445
10^7	40	$768 \times 768 \times 192$	8:8	1.015	0.813	57.965
10^7	70	768×192	8	1.238	0.557	72.436
10^7	75	768×192	8	1.283	0.293	75.657
10^7	77	2048×512	8	1.201	0.987	76.363
10^7	80	2048×512	8	1.243	1.001	78.988
10^7	100	768×192	8	1.580	1.104	94.772
10^7	200	1024×512	2	2.284	1.725	181.83
10^7	400	2048×512	4	3.830	2.962	356.98
10^7	500	1024×512	2	4.479	3.454	448.15
10^7	1000	1024×512	2	7.592	5.861	893.07
10^7	1500	1024×512	2	10.21	8.028	1349.6
10^7	2000	1024×512	2	12.69	9.999	1801.2
10^7	3000	1024×512	2	17.67	13.53	2713.6
10^8	5	1024×256	8	0.803	0.466	73.075
10^8	20	1024×512	4	0.811	0.653	79.221
10^8	120	1152×384	6	1.099	0.523	132.73
10^8	150	1152×384	6	1.229	0.439	153.65
10^8	165	1152×384	6	1.258	1.000	165.86
10^8	170	1152×384	6	1.322	1.009	169.75

build scaling laws for $H \geq H_{crit}$ that successfully describe convection for this case. This may indicate that the two convective regimes are driven by different physical processes, and that our theoretical framework only accounts for the physical processes governing
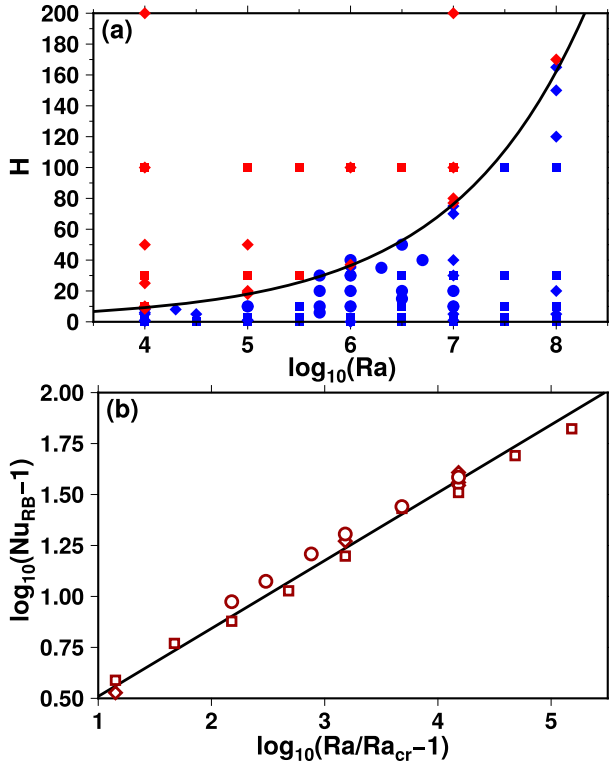
Figure 1. (a) Determination of H_{crit} as a function of Ra, blue points and red points correspond to numerical simulations with a positive and negative bottom heat flux, respectively. The black solid curve shows eq. (18) with $C_N = 1.5$. (b) Nusselt number (Nu_{RB}) as a function of the Rayleigh number (Ra) for Rayleigh–Bénard convection and free slip boundary conditions. The black solid line is the predicted scaling law (Table 1) for $C_N = 1.5$, provided that $Nu_{\mathrm{RB}} = 0.5\,H_{\mathrm{crit}}$ and following eq. (11). Circle symbols are from Sotin & Labrosse (1999), square symbols from Moore (2008) and diamond symbols show our new numerical simulations (Table 2).

mixed heating convection for $H \geq H_{\mathrm{crit}}$. In the next section, we discuss the possible physical processes that may be involved in each system.

4 MECHANISMS OF INSTABILITY

The theoretical framework developed in Section 2 is based on Howard's theory, in which thermal instabilities grow in the TBL by conductive cooling (or heating) only. In other words, the TBL is free to evolve without constraints from the convective interior. Following this theory, instabilities detach from the TBL and sink (or rise) when the Rayleigh number of the TBL (Ra_{TBL}) reaches a threshold value characterizing its own stability. The conductive growth of the TBL, therefore, defines the maximum temperature at its base. The threshold value of Ra_{TBL} does not depend on Ra, and is equal to its value for $Ra = Ra_{\mathrm{cr}}$, that is, $Ra_{\mathrm{TBL}} = Ra_{\mathrm{cr}}/16 \approx 41$ for a bottom-heated system (eq. 3) and $Ra_{\mathrm{TBL}} = Ra_{\mathrm{cr}} \approx 657$ when volumetric heating is dominant. The incapacity of our scaling laws to explain observations for $H \leq H_{\mathrm{crit}}$ may indicate that instabilities are generated by a different mechanism than conductive growth, or that the conductive growth of instabilities is perturbed by an additional mechanism. For mixed heated systems with $H \leq H_{\mathrm{crit}}$, an obvious mechanism that may alter conductive growth of instabilities is the interaction with upwellings or downwellings arriving from the opposite TBL. A simple way to identify whether additional or different mechanisms exist is to measure the thermal boundary
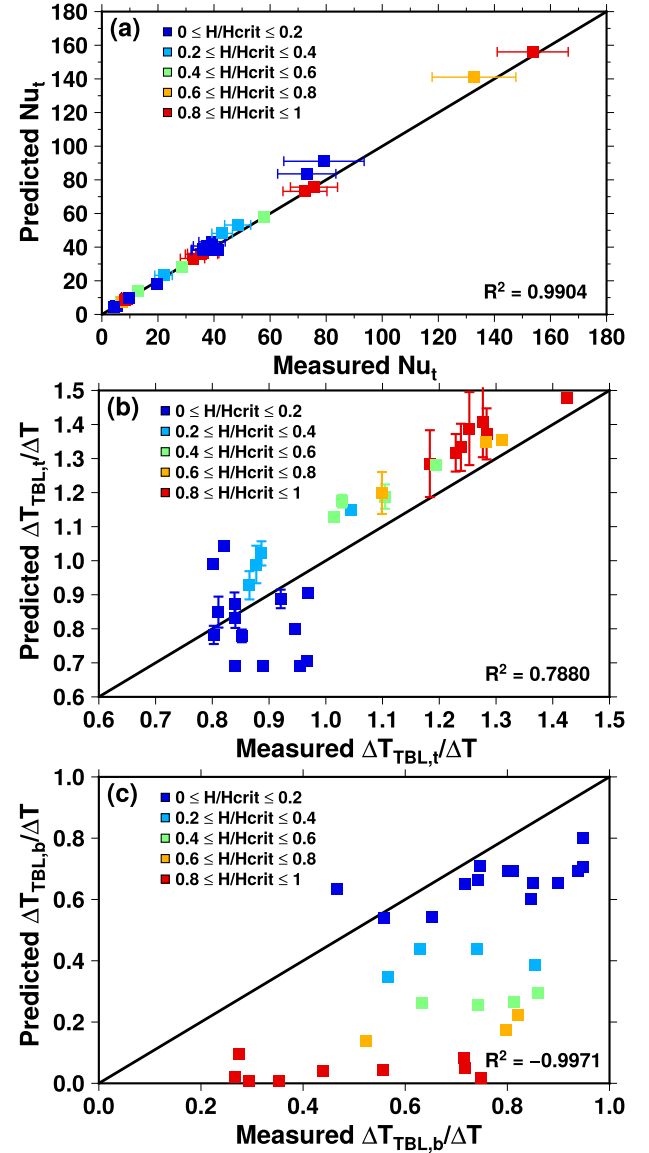

Figure 2. Comparison between predictions and measurements for (a) the dimensionless surface heat flux (Nu_{t}), (b) the dimensionless temperature jump across the top thermal boundary layer ($\Delta T_{\mathrm{TBL,\,t}}/\Delta T$), and (c) the dimensionless temperature jump across the bottom thermal boundary layer ($\Delta T_{\mathrm{TBL,\,b}}/\Delta T$) for the cases with $H \leq H_{\mathrm{crit}}$. The scaling laws used for predictions are listed in Table 1, and are given by eqs (17), (30), (36) for (a), (b), (c), respectively. The solid lines correspond to a perfect agreement between predictions and measurements, while the R^2 (eq. 43) values of the fits are indicated in each panel. Errors bars in (a) represent the temporal fluctuations of the measured Nu_{t}, which in turn induce error bars, according to eq. (30), in the prediction of $\Delta T_{\mathrm{TBL,\,t}}$. The symbol colours represent the corresponding value for H/H_{crit}.

layer Rayleigh number, Ra_{TBL}, for comparison with the theoretical values given above.

4.1 Rayleigh number of the thermal boundary layer

As a first step, we focus on the cases where volumetric heating is the dominant source of heating, that is, $H \geq H_{\mathrm{crit}}$, for two representative cases, $Ra = 10^4$ and $Ra = 10^7$. The expression of Ra_{TBL} given in
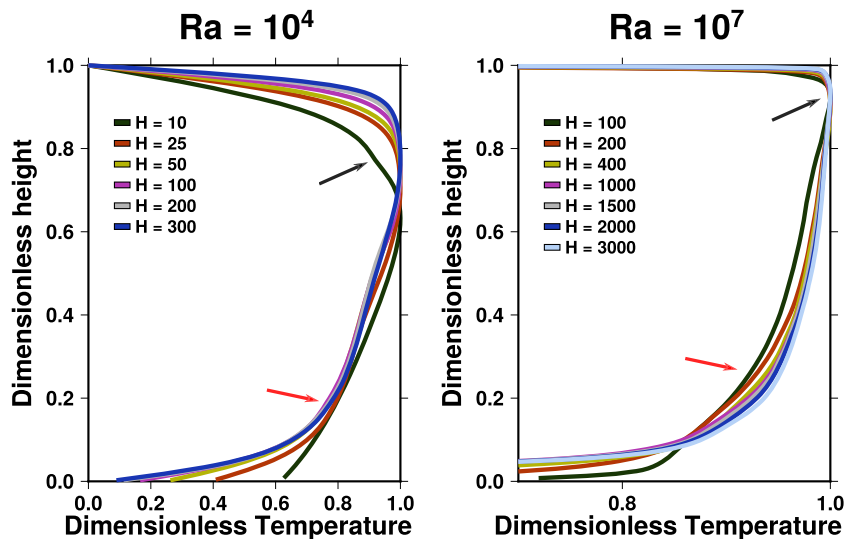
Figure 3. Horizontally averaged temperature profile for $Ra = 10^4$ and $Ra = 10^7$ considering different values of H. Temperature profiles are rescaled in a way that the maximum temperature along the profile is equal to one. This enables verifying eq. (38), which states that the ratio of the temperature at the base of the top thermal boundary layer (indicated by the black arrows) over the temperature at the top of the conductive layer (indicated by the red arrows) does not change with H.

eq. (3) can be written as

$$Ra_{\mathrm{TBL}} = Ra \, \frac{\Delta T_{\mathrm{TBL}}}{\Delta T} \left(\frac{\delta_{\mathrm{TBL}}}{d} \right)^3. \tag{44}$$

Measurements of Ra_{TBL} rely on the determination of the thickness and the temperature jump across the top TBL. Different methods for determining the base of the TBL lead to similar results in terms of temperature, but may induce dramatic change in terms of thickness. Preliminary results (described in more detail in Appendix) indicate that the definition of the TBL used in the previous section, that is, the closest point to the top surface where the first spatial derivative is smaller than 1 per cent of the minimum value along the profile, is appropriate for results at $Ra = 10^4$, but is not ideal at $Ra = 10^7$. We, therefore, adapted the method determining the base of the TBL to the value of Ra. For $Ra = 10^4$, we keep the previous definition, while, for $Ra = 10^7$, we follow a criterion based on the second spatial derivative of temperature rather than its first spatial derivative. For each numerical simulation, the value of Ra_{TBL} is averaged over time until it oscillates around a stable value, thus reducing the uncertainties. Note that the two different methods used to determine the base of the TBLs give a temperature jump across the TBL that typically differ by less than 1 per cent, which shows the robustness of the results derived in the previous section. Results are plotted in Fig. 5(a) for $Ra = 10^4$ and $Ra = 10^7$, and show small fluctuations induced by uncertainties on the measurements. When averaged over all the numerical simulations available, we find that $Ra_{\mathrm{TBL}} = 540$ and $Ra_{\mathrm{TBL}} = 580$ for $Ra = 10^4$ and $Ra = 10^7$, respectively. These values are in close agreement with the critical Rayleigh number ($Ra_{\mathrm{cr}} = 657.5$), which strongly support the validity of our theory.

As a second step, we use the same method for the cases with $H \leq H_{\mathrm{crit}}$. For cases where $0 < H \leq H_{\mathrm{crit}}$, the determination of Ra_{TBL} at $Ra = Ra_{\mathrm{cr}}$ is non-trivial. We therefore focus our reasoning on Rayleigh–Bénard convection ($H = 0$) where a theoretical prediction for Ra_{TBL} has been proposed, and assume that the conclusions can be extended to mixed heating convection with $H \leq H_{\mathrm{crit}}$. Fig. 5(b) shows that Ra_{TBL} decreases sharply with decreasing H and reaches a very low value for Rayleigh–Bénard convection. In that case, numerical simulations in 3-D Cartesian geometry indicate Ra_{TBL}

≈ 90 and $Ra_{\mathrm{TBL}} \approx 20$ for $Ra = 10^4$ and $Ra = 10^7$, respectively. These values are in clear disagreement with the theoretical value for the purely bottom-heated system, that is, $Ra_{\mathrm{cr}}/16 \approx 41$ (eq. 3). Furthermore, Sotin & Labrosse (1999) have previously conducted a similar analysis and found values for Ra_{TBL} much lower than the theoretical value, in agreement with our result at $Ra = 10^7$. This shows the complexity of the convective system when $H = 0$. As an example, we consider the case where Ra_{TBL} is much lower than its theoretical value. This suggests that either the thickness of the TBL and/or the temperature jump across it is (are) lower than the predicted value(s). Fig. 2(b) shows that in some cases the temperature jump is actually lower than the predicted value; differences are however not enough to explain the values of Ra_{TBL} previously reported. A reduction of the thickness of the TBL must, therefore, be invoked to explain the low values of Ra_{TBL}. Following a similar reasoning, one can conclude that values of Ra_{TBL} much larger than the theoretical prediction indicate an increase of the thickness of the TBL. For both cases, other mechanisms than the simple conductive growth may thus be involved in the generation of instabilities, altering this growth, and providing better explanation to the observed values of Ra_{TBL}.

4.2 Mechanisms generating instabilities

We now search for suitable mechanisms explaining the variability of Ra_{TBL} (Fig. 5b), $\Delta T_{\mathrm{TBL, t}}$ (Fig. 2b) and $\Delta T_{\mathrm{TBL, b}}$ (Fig. 2c) compared to their theoretical values when $H \leq H_{\mathrm{crit}}$. The main difference between convective regimes with $H \geq H_{\mathrm{crit}}$ and $H \leq H_{\mathrm{crit}}$ is that in the first case only one TBL is present (at the top of the system), while in the second case a second TBL (at the bottom of the system) is also present. Therefore, for $H \leq H_{\mathrm{crit}}$, the likely mechanisms influencing the growth of instabilities from the TBL may involve mechanical interactions between this TBL and hot (cold) instabilities arriving from the opposite bottom (top) TBL. Before investigating alternative mechanisms for generating instabilities, we give a brief presentation of the conductive growth with a particular emphasis on the interpretations of Ra_{TBL} values.
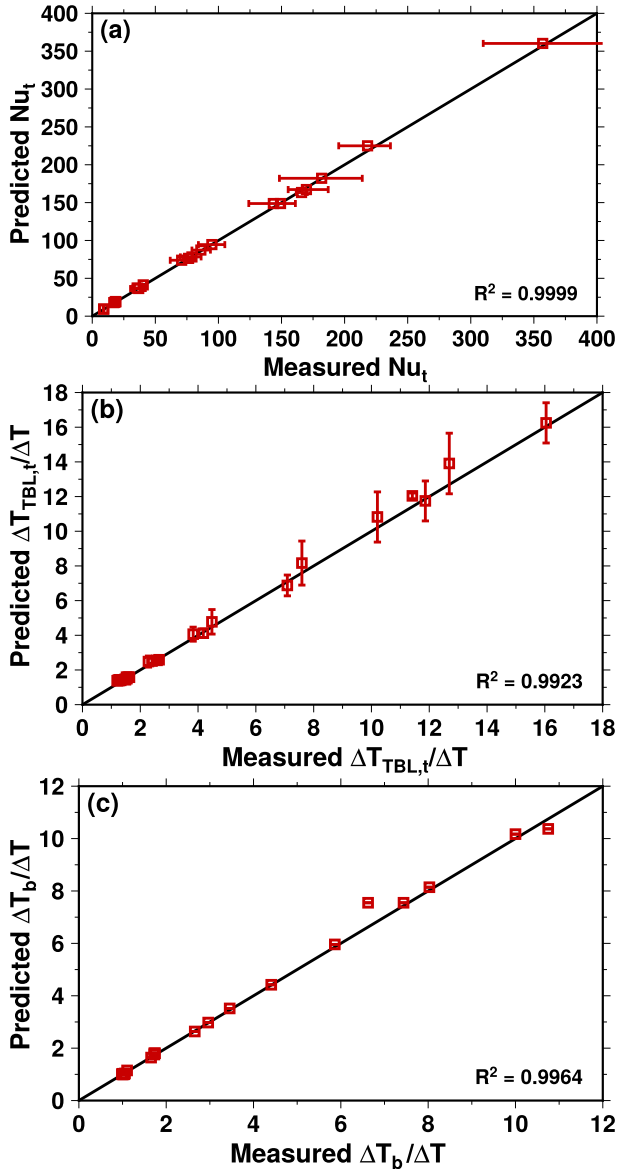
Figure 4. Comparison between predictions and measurements for (a) the dimensionless surface heat flux (Nu_t), (b) the dimensionless temperature jump across the top thermal boundary layer ($\Delta T_{TBL,\,t}/\Delta T$), and (c) the temperature jump across the convective layer ($\Delta T_b/\Delta T$), that is, between the surface and the top of the conductive layer, for the cases where $H \geq H_{crit}$. The scaling laws used for predictions are listed in Table 1. The solid lines correspond to a perfect agreement between predictions and measurements, while the R^2 (eq. 43) values of the fits are indicated in each panel. Errors bars in (a) represent the temporal fluctuations of the measured Nu_t, which in turn induce error bars, according to eq. (30), in the prediction of $\Delta T_{TBL,\,t}$.

As previously mentioned, the conductive growth of instabilities was first suggested by Howard (1966). He considered a purely bottom-heated layer of fluid with a constant temperature. In this system, the two TBLs thicken by conduction until they reach a critical threshold and break-off to generate thermal instabilities. As a result, TBLs are stable as long as Ra_{TBL} is lower than its critical value. This observation has been used to describe the stability of a convective system, with lower Ra_{TBL} indicating a more stable layer, where instabilities are less likely to be generated. However, the observation of Howard (1966) relies on a system without a well-developed convection. By contrast, when well-developed convection operates

each instability attracts material from its neighbourhood. The extent of the region affected by one particular instability defines a 'sphere of influence', in which the fluid is moving towards the instability. Within this sphere of influence, the TBL is therefore unstable and its Ra_{TBL} is larger than its critical value. Locally, however, the presence of a well-developed instability prevents the development of new ones. New instabilities are generated in the gaps between the different spheres of influence. In those gaps, Ra_{TBL} may be locally lower than its critical value, which would trigger the conductive growth of the TBL. The thermal structure of the TBL, in particular its temperature jump and thickness, then evolves following a specific conductive profile until Ra_{TBL} reaches its critical threshold, at which time an instability is generated. Several conclusions can be drawn from this description. First, instabilities for well-developed convection are more likely to be generated where Ra_{TBL} is low, which is somewhat different from the conclusion of Howard (1966). Second, the conductive growth of the TBL imposes a maximum temperature jump across this TBL corresponding to a specific thickness. Note that all the instabilities may not be generated by the conductive growth of the TBL, but, provided that the system has a large enough horizontal extent, the hot temperature profile would depict the location where the thermal structure of the TBL is imposed by this conductive growth. This explains the observation that Ra_{TBL} in a purely volumetrically heated system (Vilella & Kaminski 2017) or in a mixed heating system dominated by internal heating (Fig. 5a) is equal to Ra_{cr}.

The reasoning above assumes that the TBL is not influenced by the convective interior, which is incorrect when $H \leq H_{crit}$ because of the presence of instabilities coming from the opposite TBL. Interactions between the two TBLs have been proposed in the past (Labrosse 2002; Moore 2008), but were not clearly characterized. In order to better visualize and identify the mechanisms triggering instabilities, we conducted an additional numerical simulation of Rayleigh–Bénard convection, that is, $H = 0$, in 2-D Cartesian geometry for $Ra = 10^6$. Fig. 6 shows an example of a hot upwelling reaching the top TBL. When the hot upwelling reaches the top TBL, it induces a dramatic thinning of the TBL as well as an increase of the temperature contrast. This causes a clear decrease of Ra_{TBL}, which drops to ~10, far below the theoretical prediction $Ra_{cr}/16 \approx 41$ (eq. 3). The TBL then grows by conduction until it reaches its critical threshold, $Ra_{cr}/16 \approx 41$, generating a cold downwelling at the exact location where the hot upwelling impacted the top TBL (right panel in Fig. 6). Therefore, while the physical processes at the origin of the thermal instability are the same as those described in our theoretical framework, the thermal structure evolution of the TBL is, however, totally different. For $H \leq H_{crit}$, an impacting mechanism, as that illustrated in Fig 6, may play a key role in this evolution. Furthermore, in this 'instability impacting' mechanism, the hot temperature profile depicts the TBL at the location where the hot instability impacted the top TBL, whereas this thermal structure of the TBL is very different from the one obtained by conductive growth. In that case, the hot temperature profile provides information on the instabilities coming from the opposite TBL rather than on the TBL itself. Larger temperature jump across the TBL and smaller Ra_{TBL} are expected when the instability impacting mechanism is operating. However, because hot instabilities become weaker with increasing H, the instability impacting mechanism should only influence the result for moderate values of H. Interestingly, we measured larger $\Delta T_{TBL,\,t}$ than predicted in few cases (Fig. 2b); all of these were for H close to zero. We also measured larger $\Delta T_{TBL,\,b}$ than predicted in almost all the numerical simulations with $H \leq H_{crit}$ (Fig. 2c). In particular, the misfit becomes larger with increasing
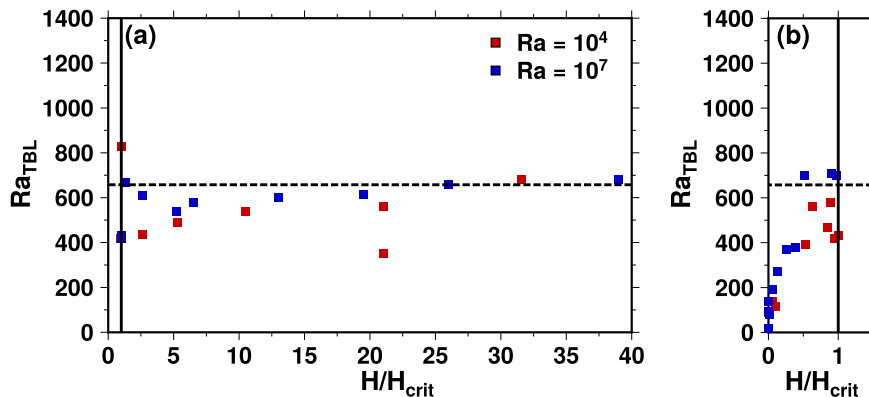
Figure 5. (a) Rayleigh number of the top thermal boundary layer (Ra_{TBL}) as a function of the ratio between the prescribed and critical heating rates (H and H_{crit}). (b) Same as panel (a), but only the values for $H/H_{crit} \leq 1$ are shown. Two values of the Rayleigh number are considered, $Ra = 10^4$ (red squares) and $Ra = 10^7$ (blue squares). In all cases, the thermal boundary layer is determined using the hot temperature profile, and its base is set as the closest point to the top surface where either the first (for $Ra = 10^4$) or the second (for $Ra = 10^7$) spatial derivative is smaller than 1 per cent of the minimum value along the profile. The horizontal dashed line corresponds to $Ra_{cr} = 657.5$, while the vertical solid line corresponds to H_{crit}.
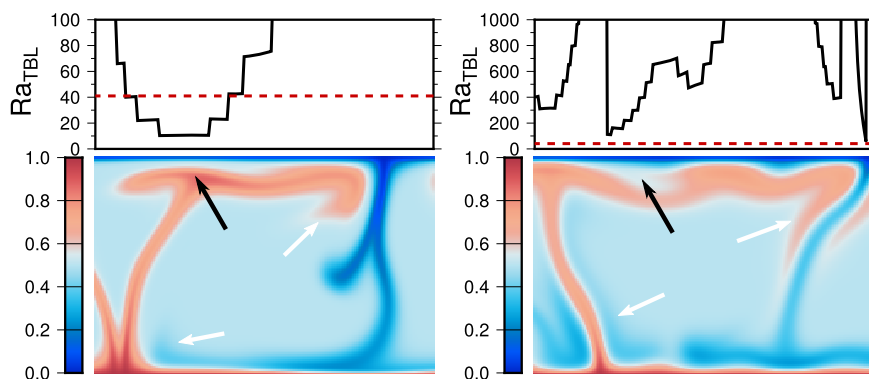
Figure 6. Details of the dimensionless temperature field (bottom panels) of a 2-D Cartesiannumerical simulation conducted for $Ra = 10^6$ and free slip top and bottom boundary conditions (for full models, see Supporting Information Fig. S2). The top panels plot the corresponding Rayleigh number of the top thermal boundary layer (Ra_{TBL}) along the horizontal direction, where the vertical axis stops either at 100 (left panel) or 1000 (right panel). On the left panel, a hot upwelling reaches the top thermal boundary layer (black arrow) reducing the thickness of the TBL and inducing a very low value of Ra_{TBL}. On the right panel, corresponding to the same location a short time after, a cold downwelling (black arrow) is generated where the hot upwelling has reached the top thermal boundary layer. The entrainment of hot (cold) instabilities by cold (hot) instabilities are shown by the white arrows.

values of H/H_{crit}, while the influence of the instability impacting mechanism is also increasing because cold downwellings become stronger. We, therefore, conclude that for all the cases in Figs 2(b) and (c), where the measured temperature jump is larger than the predicted value, instability impacting mechanism is present and alters the thermal structure of the TBL inferred from the hot temperature profile. This means that some instabilities may be generated by the conductive growth of the TBL without leaving visible features on the hot temperature profile.

Fig. 2(b) further shows results where the measured $\Delta T_{TBL,t}$ is lower than the predicted value. This cannot be explained with the instability impacting mechanism and another mechanism should be invoked. An interesting observation of this convective system is the important interior mixing when $H \leq H_{crit}$. As illustrated in Fig. 6, for $H = 0$ lateral variations in temperature are small and are mostly restricted to hot and cold instabilities. Materials located close to the top (bottom) TBL coming from hot (cold) instabilities are entrained back to the bottom (top) by cold (hot) instabilities (white arrows in Fig. 6), such that an efficient mixing occurs. This process, although weaker, can still be observed for $Ra = 10^7$ and $H = 30$ (Fig. 7a). It, however, disappears for $H \geq H_{crit}$. For instance, for $H = 2000$ (Fig. 7b) cold instabilities sink to the bottom

without being entrained back to the top, because of the absence of hot upwellings. We therefore suggest that for $H \leq H_{crit}$ the efficient interior mixing produces important lateral flow at the base of the TBL, which induces an erosion that prevents the full development of the conductive growth of the TBL, and reduces the temperature jump. This erosion mechanism explains the observed values of $\Delta T_{TBL,t}$ larger than their respective predicted value. We however expect the TBL erosion mechanism to become less important with increasing heating rates, since the mixing efficiency is reduced, as indicated by the decrease of the RMS velocity of the system (Weller *et al.* 2016). In Fig. 8, we plotted the misfit between the predicted and observed temperature jumps across the top TBL. Interestingly, this misfit strongly decreases with increasing H, reaching less than 5 per cent for $H = H_{crit}$. Considering the uncertainties inherent to the numerical simulations, for example, related to 2-D-geometry, predictions can be viewed as successful for H close to H_{crit}. Moreover, the large scattering of the misfit for values of H close to zero indicates that the three suggested mechanisms are competing with each other, such that their relative importance varies depending on the numerical simulation.

The two additional mechanisms presented in this section, that is, instability impacting and TBL erosion mechanisms, may provide
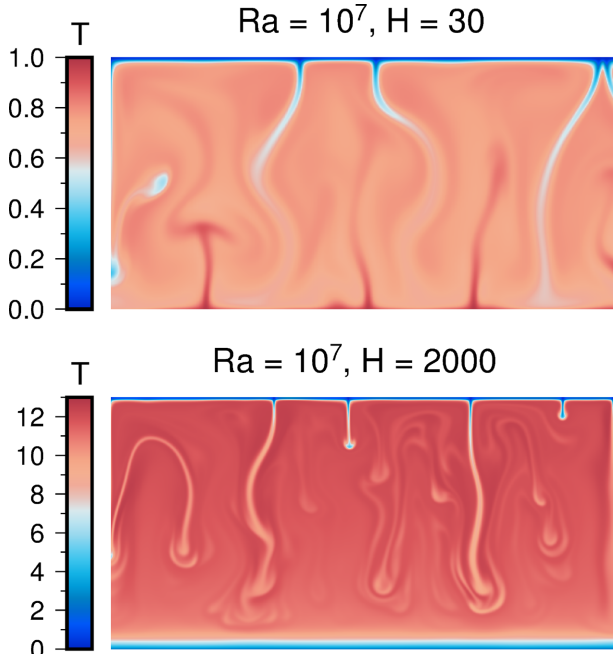
Figure 7. Details of the dimensionless temperature field of 2-D Cartesian-numerical simulations conducted for $Ra = 10^7$ with $H = 30$ (top panel) or $H = 2000$ (bottom panel). The boundary conditions are free slip at both the top and the bottom. The temperature field in the top panel is truncated to a domain aspect ratio 2, instead of 8 for the full model, in order to show the same domain aspect ratio that for the bottom panel (for the full model, see Supporting Information Fig. S3).
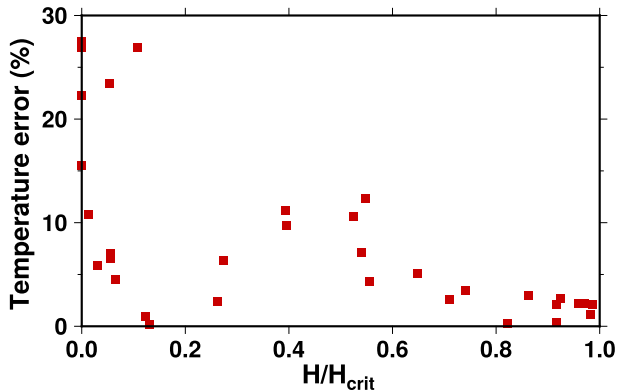

Figure 8. Misfit between the measured temperature jump across the top thermal boundary layer (TBL) and the temperature predicted by eq. (30)—as illustrated in Fig. 2b—as a function of the ratio of the heating rate (H) over the critical heating rate (H_{crit}). H/H_{crit} close to zero corresponds to the case where internal heating is negligible, while H/H_{crit} close to one corresponds to the case where bottom heating is negligible.

an explanation for the differences observed in Fig. 2. It is, however, important to keep in mind that our reasoning is only based on observations of the convective system and is, thus, mostly empirical. Theoretical modelling and quantitative studies should be conducted to describe these mechanisms in more detail and to assess their ability to characterize the convective system. This, however, is beyond the scope of this study.

5 APPLICATION TO EARLY EARTH

During the first tens of millions years of Earth's existence, our planet underwent several dramatic events. In particular, a combination of heat sources, mainly provided by planetary accretion, core formation and heat released by the decay of short-lived radionuclides ^{26}Al and ^{60}Fe, is believed to have induced a total or partial melting of the Earth's mantle (Tonks & Melosh 1993; Elkins-Tanton 2012). This event, usually referred to as the magma ocean period, sets the initial condition for the thermal evolution of the Earth's mantle, so that its good description is important for a better understanding of its subsequent evolution and current properties. For instance, the initial compositional structure is crucial for explaining the presence of hidden reservoirs of primitive undegassed material in today's deep mantle, as suggested by the high ^{142}Nd/^{144}Nd ratios (Hofmann 1997; Boyet & Carlson 2006), by the dispersion of the helium isotopic ratio, ^{3}He/^{4}He, in ocean island basalts (Lupton & Craig 1975; Farley *et al.* 1992) or by the anomalies in ^{182}W compared to mantle standard (Touboul *et al.* 2012; Puchtel *et al.* 2013; Rizo *et al.* 2016). Elkins-Tanton (2008) proposed that, at the end of the magma ocean solidification, the density profile leads to an unstable situation. This requires a subsequent complete mantle overturn to produce a stable density structure. Alternatively, Maurice *et al.* (2017) found that convection in the solidified mantle may have started before the complete solidification of the magma ocean. In that case, the solidified mantle would have mixed progressively during its solidification and a complete overturn would, therefore, not be required. A key issue, however, is to explain the presence of distinct primitive reservoir within the contemporary mantle. Here, we propose that during the solidification of the magma ocean, the heating of the solidified mantle was dominated by volumetric heating, because of the heat released by ^{26}Al and ^{60}Fe. In that case, and as illustrated by Fig. 3, the maximum temperature of the mantle would not be found at the base of the mantle but within the solidified mantle, inducing an important quantity of melt in this region. Afterwards, as the mantle cooled down, this melt should have solidified forming material enriched in iron, and therefore denser than the ambient mantle. If this material was dense enough, that is, the melt was sufficiently enriched in iron, it may have produced distinct undegassed reservoirs at the base of the mantle that have remained unmixed until today (e.g. Li *et al.* 2014). This hypothesis is somewhat similar to the model proposed by Labrosse *et al.* (2007), except that in our case the primitive reservoir has been melted twice.

To assess the relevance of our proposition, we estimated the value of both H_{crit} and the volumetric heating rate of the solidified mantle, H_m, as a function of the vertical extent of the solidified mantle, d_m. A schematic illustration of our model is shown in Fig. 9(a). The calculation of H_{crit} relies on the determination of the Rayleigh number of the solidified mantle (eq. 18), which is itself a function of the properties of the solidified mantle (assumed values are listed in Table 3), d_m (input parameter of the model), and the temperature jump across the solidified mantle, $\Delta T_m = T_{CMB} - T_{int}$, with T_{CMB} and T_{int} being the temperatures at the core–mantle boundary and at the interface between the solidified mantle and the magma ocean, respectively. To quantify ΔT_m, we further assume that both T_{int} and T_{CMB} are given by the mantle solidus temperature. Solidus as a function of depth (pressure) depends on the exact composition. For the sake of simplicity, we use a solidus profile compiled from different experimental studies of peridotites (Zhang & Herzberg 1994; Hirschmann 2000; Andrault *et al.* 2011). We further assumed that H_m is related to the heat released by the decay of ^{26}Al and ^{60}Fe and is calculated using the parameters given by Šrámek *et al.* (2012). The value of
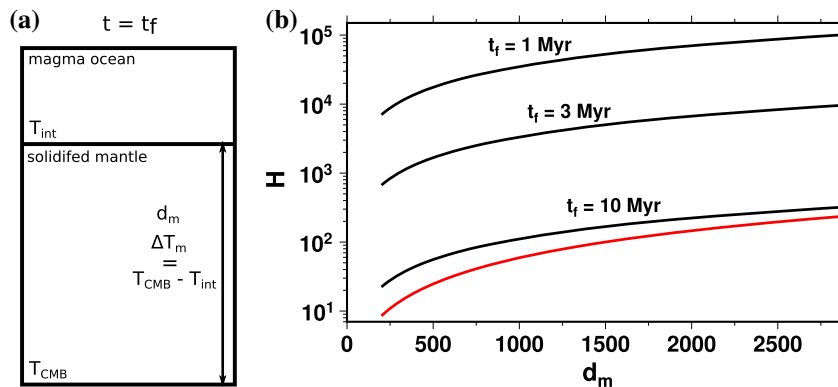
Figure 9. (a) Schematic illustration of our magma ocean cooling model at a time $t = t_f$, where t_f is the time elapsed after the solar system formation. The solidified mantle extends over a distance d_m and is characterized by a temperature jump $\Delta T_m = T_{CMB} - T_{int}$, T_{CMB} and T_{int} being the temperature at the core–mantle boundary (CMB) and at the interface between the magma ocean and the solidified mantle, respectively. (b) Black solid lines correspond to the heating rate of the solidified mantle (H_m) as a function of d_m calculated for different values of t_f. Red solid line corresponds to the critical value of H_m as a function of d_m.

Table 3. Parameters used to model the solidified mantle during the magma ocean cooling.

Symbol	Unit	Description	Value
ρ	kg m^{-3}	Density	4400
α	K^{-1}	Thermal expansion coefficient	10^{-5}
λ	W m^{-1} K^{-1}	Thermal conductivity	5
κ	m^2 s^{-1}	Thermal diffusivity	10^{-6}
g	m s^{-2}	Acceleration of gravity	10
η	Pa s	Viscosity	10^{20}

H_m depends on both d_m and the time elapsed after the solar system formation (i.e. after the crystallization of calcium–aluminium inclusions), t_f. Models of magma ocean evolution (Lebrun *et al.* 2013; Salvador *et al.* 2017) indicate a cooling time of the order of 1 Myr. However, because the cooling time of the magma ocean and the timing of this event remain poorly constrained, we considered three representative values for t_f, $t_f = 1$ Myr, $t_f = 3$ Myr and $t_f = 10$ Myr. Fig. 9(b) plots H_{crit} and H_m as a function of d_m. We found that, for a given value of d_m, H_m decreases with t_f. More interestingly, H_m remains larger than H_{crit} even for $t_f = 10$ Myr. In other words, during the magma ocean cooling process the heating rate in the solidified mantle may be such that the maximum temperature is reached within the solid mantle, which in turn may indicate the generation of a significant amount of melting within the solidified mantle.

One should, however, keep in mind that these results rely on several important assumptions. First, they are valid for steady-state convection, while properties of the solidified mantle, especially its thickness, are changing with time. The typical amount of time with which these properties are varying scales approximately as the cooling time of the magma ocean. If this time is large compared to the typical time for convection, the convective system can be considered in steady state, and our scaling laws may be applied. In the opposite case, the convective system remains in a transitional regime, and our scaling laws may not be applied. Unfortunately, there is, to date, no constraint that would allow discriminating between these two possibilities. In addition, the behaviour of scaling laws during transitional regimes remains to be investigated. Second, we assumed that the abundances of radioactive isotopes in the solidified mantle were the same as those in the bulk mantle, that is, the combination of the magma ocean and the solidified mantle. Radioactive isotopes, however, may have been partitioned between

the liquid and solid phases. The exact partitioning depends on the mechanism for magma ocean cooling (Elkins-Tanton 2012) and is difficult to estimate. Moreover, the abundances of radioactive isotopes also depends on the time elapsed after the solar system formation, which is not well constrained (e.g. Touboul *et al.* 2012). If the magma ocean period occurred much later than 10 Myr, then the short-lived radioactive isotopes would already be extinct impacting our conclusions importantly. Third, H_{crit} has been determined here for a Cartesian geometry, whereas the Earth's mantle is spherical. Spherical geometry would increase the value of H_{crit} (O'Farrell & Lowman 2010) and therefore makes the occurrence of melting more difficult. Finally, the method used here, based on scaling laws, neglects many complexities such as the effect of the variation of fluid properties, in particular variations of viscosity with temperature and grain size. Variations of temperature are relatively modest for low values of d_m but becomes important at the end of the magma ocean stage. In that case, convection in the solidified mantle may operate in a so-called 'stagnant-lid regime' (e.g. Davaille & Jaupart 1993; Moresi & Solomatov 1995), in which large variations of viscosity with temperature lead to the formation of a top conductive layer where vertical and horizontal flows are inhibited. In addition, viscosity varies importantly with the grain size (e.g. Karato & Wu 1993), which itself may change with space and time. In particular, it has been suggested that the cooling process of the magma ocean evolves with time (Elkins-Tanton 2012; Ballmer *et al.* 2017), and this evolution may, in turn, lead to variations in grain size. Although the variations of viscosity with temperature and grain size remain a matter of debate, these variations, together with the complexities we discussed above, must certainly have had a strong influence that impacted, importantly, the thermal convection in early Earth. However, all these complexities will probably not change the value of

H_{crit} by several orders of magnitude such that the maximum temperature may still be expected to occur within the solidified mantle. Furthermore, compressibility effects imply a progressive increase of temperature with depth. This, together with the typical temperature profile shown in Fig. 3, indicates that the maximum temperature may be localized close to the bottom, inducing a local generation of melting.

Complex numerical simulations of diphasic flow, similar to those performed by Ulvrová *et al.* (2012), are further required to investigate our scenario in detail. In particular, it is important to further quantify the amount and localization of the melting, since in our approach melting is only inferred from the value of the heating rate. Again, it is also important to keep in mind that the exact value of t_f is largely unknown, while impacting our conclusions importantly. Stronger constraints on the different events occurring during the early Earth are crucial to establish a robust scenario of this period. Despite these limitations, the model we propose here has the advantage to reconcile current understanding of magma ocean dynamics and geochemical observations pointing to the presence of a primitive undegassed reservoir in today's Earth mantle.

6 CONCLUSION

We have developed theoretical scaling laws for the temperature jump across the TBL(s) and the surface heat flux of convecting systems with mixed heating. The scaling laws for Rayleigh–Bénard convection and for mixed heating convection for H lower than a threshold value H_{crit}, defined as the amount of internal heating for which the bottom heat flux changes sign, from positive ($H \leq H_{\mathrm{crit}}$) to negative ($H \geq H_{\mathrm{crit}}$), failed to predict the temperature jump across the TBL. We argued that this failure is caused by different competing ways to generate and grow instabilities. More precisely, the conductive growth of instabilities, which operates in purely internally heated systems, also occurs in mixed heated systems with $H \leq H_{\mathrm{crit}}$, but is altered by interactions with instabilities (upwellings or downwellings) coming from the opposite TBL. Conductive growth is cut short, and instabilities are more easily generated. The scaling laws in mixed heating convection for H larger than H_{crit} are, however, in excellent agreement with measurements, validating, in this case, a pure conductive growth as the only mechanism driving the development of instabilities. These results clearly show that different mechanisms of destabilization are operating in TBLs, and that the classical theory of Howard (1966) is only valid when $H \geq H_{\mathrm{crit}}$. Application of our results to the cooling of the early Earth magma ocean may suggest that convection in the solidified part of the mantle was dominated by volumetric heating. In that case, large quantities of melt would have been produced close to the interface with the core, leading to the formation of distinct reservoirs of primitive undegassed material in today's Earth mantle, as that advocated by several geochemical observations. This scenario may stand as a coherent model for explaining the evolution of the early Earth.

REFERENCES

Andrault, D., Bolfan-Casanova, N., Lo Nigro, G., Bouhifd, M.A., Garbarino, G. & Mezouar, M., 2011. Solidus and liquidus profiles of chondritic mantle: implication for melting of the Earth across its history, *Earth planet. Sci. Lett.,* **304,** 251–259.

Ballmer, M.D., Lourenço, D.L., Hirose, K., Caracas, R. & Nomura, R., 2017. Reconciling magma-ocean crystallization models with the present-day structure of the Earth's mantle, *Geochem., Geophys., Geosyst.,* **18,** 2785–2806.

Baumgardner, J.R., 1985. Three-dimensional treatment of convective flow in the earth's mantle, *J. Stat. Phys.,* **39,** 501–511.

Boyet, M. & Carlson, R.W., 2006. A new geochemical model for the Earth's mantle inferred from (SM)-S-146-Nd-142 systematics, *Earth planet. Sci. Lett.,* **250,** 254–268.

Chandrasekhar, S., 1961. *Hydrodynamic and Hydromagnetic Stability,* Clarendo Press.

Choblet, G., 2012. On the scaling of heat transfer for mixed heating convection in a spherical shell, *Phys. Earth planet. Inter.,* **206–207,** 31–42.

Choblet, G. & Parmentier, E.M., 2009. Thermal convection heated both volumetrically and from below: implications for predictions of planetary evolution, *Phys. Earth planet. Inter.,* **173,** 290–296.

Christensen, U.R., 1985. Thermal evolution models for the Earth, *J. geophys. Res.,* **90,** 2995–3007.

Christensen, U.R. & Hofmann, A.W., 1994. Segregation of subducted oceanic crust in the convecting mantle, *J. geophys. Res.,* **99,** 19 867–19 884.

Cross, M.C. & Hohenberg, P.C., 1993. Pattern formation outside of equilibrium, *Rev. Mod. Phys.,* **65**(3), 851.

Daly, S.F., 1980. Convection with decaying heat sources: constant viscosity, *Geophys. J. R. astr. Soc.,* **61,** 519–247.

Davaille, A. & Jaupart, C., 1993. Transient high-Rayleigh-number thermal convection with large viscosity variation, *J. Fluid Mech.,* **253,** 141–166.

Deschamps, F., Tackley, P.J. & Nakagawa, T., 2010. Temperature and heat flux scalings for isoviscous thermal convection in spherical geometry, *Geophys. J. Int.,* **182,** 137–154.

Deschamps, F., Li, Y. & Tackley, P.J., 2015. *Large-Scale Thermo-chemical Structure of the Deep Mantle: Observations and Models,* pp. 479–515, Springer International Publishing.

Elkins-Tanton, L.T., 2008. Linked magma ocean solidification and atmospheric growth for Earth and Mars, *Earth planet. Sci. Lett.,* **271,** 181–191.

Elkins-Tanton, L.T., 2012. Magma Oceans in the Inner Solar System, *Annu. Rev. Earth Planet. Sci.,* **40,** 113–139.

Farley, K.A., Natland, J.H. & Craig, H., 1992. Binary mixing of enriched and undegassed (primitive?) mantle components (He, Sr, Nd, Pb) in Samoan lavas, *Earth planet. Sci. Lett.,* **111,** 183–199.

Galsa, A. & Lenkey, L., 2007. Quantitative investigation of physical properties of mantle plumes in three-dimensional numerical models, *Phys. Fluids,* **19,** 116601, doi:10.1063/1.2794284.

Hirschmann, M.M., 2000. Mantle solidus: experimental constraints and the effects of peridotite composition, *Geochem. Geophys.Geosyst.,* **1,** doi:10.1029/2000GC000070.

Hofmann, A.W., 1997. Mantle geochemistry: the message from oceanic volcanism, *Nature,* **385,** 219–229.

Howard, L.N., 1966. Convection at high Rayleigh number, in *Proceedings of the 11th International Congress on Applied Mechanics,* pp. 1109–1115, Springer-Verlag, New York.

Jarvis, G.T., Glatzmaier, G.A. & Vangelov, V.I., 1995. Effects of curvature, aspect ratio and plan form in two- and three-dimensional spherical models of thermal convection, *Geophys. Astrophys. Fluid Dyn.,* **79,** 147–171.

Jaupart, C., Labrosse, S., Lucazeau, F. & Mareschal, J.C., 2015. *Temperatures, Heat and Energy in the Mantle of the Earth, Treatise on Geophysics,* Vol. **7,** pp. 223–270, Elsevier.

Jeanloz, R. & Morris, S., 1987. Is the mantle geotherm subadiabatic? *Geophys. Res. Lett.,* **14,** 335–338.

Jellinek, A.M. & Jackson, M.G., 2015. Connections between the bulk composition, geodynamics and habitability of Earth, *Nat. Geosci.,* **8,** 587–593.

Karato, S.I. & Wu, P., 1993. Rheology of the upper mantle: a synthesis, *Science,* **260,** 771–778.

Kite, E.S., Manga, M. & Gaidos, E., 2009. Geodynamics and rate of volcanism on massive Earth-like planets, *Astrophys. J.,* **700,** 1732–1749.

Krishnamurti, R., 1968. Finite amplitude convection with changing mean temperature. Part 1. Theory, *J. Fluid Mech.,* **33,** 445–455.

Labrosse, S., 2002. Hotspots, mantle plumes and core heat loss, *Earth planet. Sci. Lett.,* **199,** 147–156.

Labrosse, S., Hernlund, J.W. & Coltice, N., 2007. A crystallizing dense magma ocean at the base of the Earth's mantle, *Nature,* **450,** 866–869.

Laneuville, M., Wieczorek, M.A., Breuer, D. & Tosi, N., 2013. Asymmetric thermal evolution of the Moon, *J. geophys. Res.,* **118,** 1435–1452.

Lebrun, T., Massol, H., Chassefière, E., Davaille, A., Marcq, E., Sarda, P., Leblanc, F. & Brandeis, G., 2013. Thermal evolution of an early magma ocean in interaction with the atmosphere, *J. geophys. Res.,* **118,** 1155–1176.

Li, Y., Deschamps, F. & Tackley, P.J., 2014. The stability and structure of primordial reservoirs in the lower mantle: insights from models of thermochemical convection in three-dimensional spherical geometry, *Geophys. J. Int.,* **199,** 914–930.

Liu, X. & Zhong, S., 2013. Analyses of marginal stability, heat transfer and boundary layer properties for thermal convection in a compressible fluid with infinite Prandtl number, *Geophys. J. Int.,* **194,** 125–144.

Lupton, J.E. & Craig, H., 1975. Excess ^{3}He in oceanic basalts: Evidence for terrestrial primordial helium, *Earth planet. Sci. Lett.,* **26,** 133–139.

Machetel, P. & Yuen, D.A., 1989. Penetrative convective flows induced by internal heating and mantle compressibility, *J. geophys. Res.,* **94,** 10 609–10 626.

Malkus, W. V.R., 1954. Discrete Transitions in Turbulent Convection, *Proc. Royal Soc. Lond.,* **225,** 185–195.

Maurice, M., Tosi, N., Samuel, H., Plesa, A.-C., Hüttig, C. & Breuer, D., 2017. Onset of solid-state mantle convection and mixing during magma ocean solidification, *J. geophys. Res.,* **122,** 577–598.

McKenzie, D.P., Roberts, J.M. & Weiss, N.O., 1973. Numerical models of convection in the earth's mantle, *Tectonophysics,* **19,** 89–103.

Moore, W.B., 2008. Heat transport in a convecting layer heated from within and below, *J. geophys. Res.,* **113,** B11407, doi:10.1029/2006JB004778 .

Moresi, L.N. & Solomatov, V.S., 1995. Numerical investigation of 2D convection with extremely large viscosity variations, *Phys. Fluids,* **7,** 2154–2162.

O'Farrell, K.A. & Lowman, J.P., 2010. Emulating the thermal structure of spherical shell convection in plane-layer geometry mantle convection models, *Phys. Earth planet. Inter.,* **182,** 73–84.

O'Farrell, K.A., Lowman, J.P. & Bunge, H.-P., 2013. Comparison of spherical-shell and plane-layer mantle convection thermal structure in viscously stratified models with mixed-mode heating: implications for the incorporation of temperature-dependent parameters, *Geophys. J. Int.,* **192,** 456–472.

Ogawa, M., Schubert, G. & Zebib, A., 1991. Numerical simulations of three-dimensional thermal convection in a fluid with strongly temperature-dependent viscosity, *J. Fluid Mech.,* **233,** 299–328.

Parmentier, E.M. & Sotin, C., 2000. Three-dimensional numerical experiments on thermal convection in a very viscous fluid: Implications for the dynamics of a thermal boundary layer at high Rayleigh number, *Phys. Fluids,* **12,** 609–617.

Parmentier, E.M., Sotin, C. & Travis, B.J., 1994. Turbulent 3-D thermal convection in an infinite Prandtl number, volumetrically heated fluid: implications for mantle dynamics, *Geophys. J. Int.,* **116,** 241–251.

Puchtel, I.S., Blichert-Toft, J., Touboul, M., Walker, R.J., Byerly, G.R., Nisbet, E.G. & Anhaeusser, C.R., 2013. Insights into early Earth from Barberton komatiites: Evidence from lithophile isotope and trace element systematics, *Geochim. Cosmochim. Acta,* **108,** 63–90.

Rizo, H., Walker, R.J., Carlson, R.W., Horan, M.F., Mukhopadhyay, S., Manthos, V., Francis, D. & Jackson, M.G., 2016. Preservation of Earth-forming events in the tungsten isotopic composition of modern flood basalts, *Science,* **352,** 809–812.

Salvador, A., Massol, H., Davaille, A., Marcq, E., Sarda, P. & Chassefière, E., 2017. The relative influence of H_2O and CO_2 on the primitive surface conditions and evolution of rocky planets, *J. geophys. Res.,* **122,** 1458–1486.

Shahnas, M.H., Lowman, J.P., Jarvis, G.T. & Bunge, H.P., 2008. Convection in a spherical shell heated by an isothermal core and internal sources: Implications for the thermal state of planetary mantles, *Phys. Earth planet. Inter.,* **168,** 6–15.

Sharpe, H. & Peltier, W.R., 1978. Parameterized mantle convection and the Earth's thermal history, *Geophys. Res. Lett.,* **5,** 737–740.

Silveston, P.L., 1958. Wärmedurchgang in waagerechten Flüssigkeitsschichten, *Forschung auf dem Gebiet des Ingenieurwesens A,* **24,** 59–69.

Sinha, G. & Butler, S.L., 2007. On the origin and significance of subadiabatic temper ature gradients in the mantle, *J. geophys. Res.,* **112,** B10406, doi:10.1029/2006JB004850.

Solomatov, V.S. & Moresi, L.N., 2000. Scaling of time-dependent stagnant lid convection: Application to small-scale convection on Earth and other terrestrial planets, *J. geophys. Res.,* **105,** 21795–21817.

Sotin, C. & Labrosse, S., 1999. Three-dimensional thermal convection in an iso-viscous, infinite Prandtl number fluid heated from within and from below: applications to the transfer of heat through planetary mantles, *Phys. Earth planet. Int.,* **112,** 171–190.

Šrámek, O., Milelli, L., Ricard, Y. & Labrosse, S., 2012. Thermal evolution and differentiation of planetesimals and planetary embryos, *Icarus,* **217,** 339–354.

Tackley, P.J., 1996. Effects of strongly variable viscosity on three-dimensional compressible convection in planetary mantles, *J. geophys. Res.,* **101,** 3311–3332.

Tackley, P.J., 2008. Modelling compressible mantle convection with large viscosity contrasts in a three-dimensional spherical shell using the yin-yang grid, *Phys. Earth planet. Inter.,* **171,** 7–18.

Tackley, P.J., Stevenson, D.J., Glatzmaier, G.A. & Schubert, G., 1994. Effects of multiple phase transitions in a 3-dimensional spherical model of convection in Earth's mantle, *J. geophys. Res.,* **99,** 15 877–15 901.

Tonks, W.B. & Melosh, H.J., 1993. Magma ocean formation due to giant impacts, *J. geophys. Res.,* **98,** 5319–5333.

Touboul, M., Puchtel, I.S. & Walker, R.J., 2012. ^{182}W evidence for long-term preservation of early mantle differentiation products, *Science,* **335,** 1065–1069.

Townsend, A.A., 1964. Natural convection in water over an ice surface, *Q. J. R. Meteorol. Soc.,* **90,** 248–259.

Travis, B. & Olson, P., 1994. Convection with internal heat sources and thermal turbulence in the Earth's mantle, *Geophys. J. Int.,* **118,** 1–19.

Turcotte, D.L. & Oxburgh, E.R., 1967. Finite amplitude convective cells and continental drift, *J. Fluid Mech.,* **28**(1), 29–42.

Ulvrová, M., Labrosse, S., Coltice, N., Råback, P. & Tackley, P.J., 2012. Numerical modelling of convection interacting with a melting and solidification front: application to the thermal evolution of the basal magma ocean, *Phys. Earth planet. Inter.,* **206–207,** 51–66.

Vangelov, V.I. & Jarvis, G.T., 1994. Geometrical effects of curvature in axisymmetric spherical models of mantle convection, *J. geophys. Res.,* **99,** 9345–9358.

Vilella, K. & Kaminski, E., 2017. Fully determined scaling laws for volumetrically heated convective systems, a tool for assessing habitability of exoplanets, *Phys. Earth planet. Inter.,* **266,** 18–28.

Weinstein, S.A. & Olson, P., 1990. Planforms in thermal convection with internal heat sources at large Rayleigh and Prandtl numbers, *Geophys. Res. Lett.,* **3,** 239–242.

Weller, M.B., Lenardic, A. & Moore, W.B., 2016. Scaling relationships and physics for mixed heating convection in planetary interiors: Isoviscous spherical shells, *J. geophys. Res.,* **121,** 7598–7617.

Zhang, J. & Herzberg, C., 1994. Melting experiments on anhydrous peridotite KLB-1 from 5.0 to 22.5 GPa, *J. geophys. Res.,* **99,** 17 729–17 742.

Zhong, S., 2005. Dynamics of thermal plumes in three-dimensional isoviscous thermal convection, *Geophys. J. Int.,* **162,** 289–300.

SUPPORTING INFORMATION

Supplementary data are available at *GJI* online.

Figure S1. Comparison between predictions and measurements for (a and b) the dimensionless surface heat flux (Nu_t), (c and d) the dimensionless temperature jump across the top thermal boundary layer ($\Delta T_{\mathrm{TBL,t}}/\Delta T$) and (e and f) the temperature jump across the bottom thermal boundary layer ($\Delta T_{\mathrm{TBL,b}}/\Delta T$), for the cases where $H \leq H_{\mathrm{crit}}$ and $H \geq H_{\mathrm{crit}}$, respectively. The scaling laws used for predictions are from Moore (2008). The solid lines correspond to a perfect agreement between predictions and measurements, while the R^2 values of the fits are indicated in each panel. The symbol colours in the left panels represent the corresponding value for Ra.

Figure S2. Dimensionless temperature fields of a 2-D Cartesiannumerical simulation conducted for $Ra = 10^6$ and free slip top and bottom boundary conditions. The two temperature fields are separated by a short time, the top panel being earlier than the bottom one, and are used in Fig. 6.

Figure S3. Dimensionless temperature fields of a 2-D Cartesiannumerical simulation conducted for $Ra = 10^7$, $H = 30$ and free slip top and bottom boundary conditions. This temperature field is used in Fig. 7.

Please note: Oxford University Press is not responsible for the content or functionality of any supporting materials supplied by the authors. Any queries (other than missing material) should be directed to the corresponding author for the paper.

APPENDIX: DEFINITION OF THERMAL BOUNDARY LAYERS

Because the TBL does not have any precise definition, different methods have been used to define its base. In this study, we define the base of the TBL as the point where conduction becomes negligible. Here, we numerically identify this depth with the closest point to the top surface where the first spatial derivative (T') is smaller than 1 per cent of the minimum value along the profile. For instance, for the top TBL, this corresponds to the largest value of the dimensionless height z for which $T'(z) > 0.01 \min(T')$. This definition has the advantage to be fully coherent with the scaling analysis we have developed in this study. Fig. A1 shows the measured Ra_{TBL} as a function of the heating rate using this method. A striking result is the large scattering for $H/H_{\mathrm{crit}} \approx 1$, that is, for systems analogue to a purely volumetrically heated system. Vilella & Kaminski (2017) previously noted the difficulty to estimate the thickness of the TBL in the purely volumetrically heated case. To overcome this issue, they used the second spatial derivative of temperature rather than its first spatial derivative, arguing that, for this case, it provides a more accurate estimate of the TBL. We, therefore, follow this definition and we found a smaller scattering in Fig. 5. Note that the conclusions are equivalent using both definition, that is, Ra_{TBL} increases sharply with the heating rate for $H \leq H_{\mathrm{crit}}$, while it remains almost stable for $H \geq H_{\mathrm{crit}}$. A notable difference, however, is that the average value of Ra_{TBL} for $H \geq H_{\mathrm{crit}}$ is around 400 with the first method (Fig. A1), and 580 with the second method (Fig. 5). Interestingly, this latter value is very close to that of the critical Rayleigh number, $Ra_{\mathrm{cr}} = 657.5$.
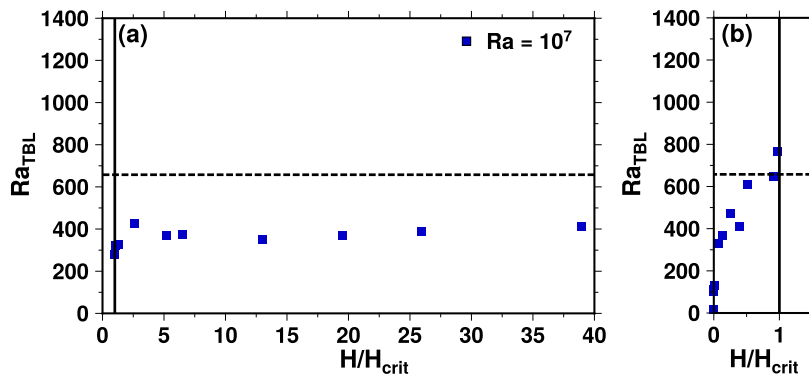

Figure A1. (a) Rayleigh number of the top thermal boundary layer (Ra_{TBL}) as a function of the ratio between the prescribed and critical heating rates (H and H_{crit}) for numerical simulations conducted with $Ra = 10^7$. (b) Same as panel (a), but only the values for $H/H_{\mathrm{crit}} \leq 1$ are shown. In all cases, the thermal boundary layer is determined using the hot temperature profile, and its base is set as the closest point to the top surface where the first spatial derivative is smaller than 1 per cent of the minimum value along the profile. The horizontal dashed line corresponds to $Ra_{\mathrm{cr}} = 657.5$, while the vertical solid line corresponds to H_{crit}.